To the Graduate Council:

I am submitting herewith a thesis written by Matthew Scott Anderson entitled "The Effect of Laser Beam Defocusing on Processing Quality During Laser Surface Alloying." I have examined the final copy of the thesis for form and content and recommend that it be accepted in partial fulfillment of the requirements for the degree of Master of Science, with a major in Engineering Science.

John A. Hopkins, Major Professor

We have read this thesis
and recommend its acceptance:

Roy J. Schulz

Mary H McCay

Accepted for the Council:

Vice Provost and Dean of Graduate Studies

THE EFFECT OF LASER BEAM DEFOCUSING ON PROCESSING QUALITY DURING LASER SURFACE ALLOYING

A Thesis
Presented for the
Master of Science
Degree
The University of Tennessee, Knoxville

Matthew Scott Anderson
December 2001

DEDICATION

This work is dedicated to my

parents and brother.

Without their support and assistance,

the completion of this thesis

would not have been possible.

ACKNOWLEDGEMENTS

I would like to thank the faculty and staff of UTSI. My thesis committee in particular has been of great assistance. Committee members include Dr. John Hopkins, Dr. Mary Helen McCay, and Dr. Roy Schulz. A special appreciation also goes to the CLA staff including Diane Chellstorp, Fred Schwartz, Newton Wright, Doug Warnberg, and Kate Lansford.

ABSTRACT

The effect on final processing quality resulting from a deviation from optimum beam focus during laser surface alloying has been investigated in this research. An elliptical laser beam was used to experimentally process samples, which were then analyzed to determine processing characteristics such as melt depth. A linear relationship was found between the melt and heat affected zone depths and defocus distance, which was −13.3 μm/mm for the melt depth and −22.3 μm/mm for heat affected zone. The dynamics of an automated focus correction were investigated, and a required vertical velocity of 4000 mm/min was needed to correct a defocus distance of −4 mm. The maximum surface variation radius was found to require a horizontal resolution 3.5 times the radius. Finally, a simple moving source analytical heat flow model, which can approximate an elliptical laser beam, was examined and shown to be unsuitable for feedback control applications under the conditions of this study.

TABLE OF CONTENTS

CHAPTER PAGE

LIST OF TABLES

LIST OF FIGURES

FIGURE PAGE

FIGURE | PAGE

NOMENCLATURE

A	surface absorptivity
A_1	A_1 transformation temperature (K)
a	thermal diffusivity (m^2s^{-1})
b	laser beam spot diameter (m)
C	specific heat (J $kg^{-1}K^{-1}$)
d	distance from lens (m)
f	focal length of lens (m)
l	length of rectangular beam parallel to direction of beam velocity (m)
L_f	latent heat of fusion (J)
P	beam power (W)
q	beam power (W)
R	aspect ratio of rectangular beam
r	radial distance from beam (m)
r_B	radius of Gaussian beam (m)
r_v	surface variation radius (m)
r_1	input beam radius (m)
r_2	output beam radius (m)
T	temperature (K)
T_m	melt temperature (K)
T_0	initial temperature (K)
T_p	peak temperature (K)

T_s	surface temperature (K)
t	time (s)
t_p	time to peak temperature (s)
v	beam velocity (m s^{-1})
w	width of rectangular beam normal to beam velocity (m)
x, y, z	Cartesian coordinates with origin at beam center (m)
z_o	characteristic length (m)
λ	thermal conductivity (J $s^{-1}m^{-1}K^{-1}$)
ρ	density (kg m^{-3})

Dimensionless Variable Definitions

$T^* = (T - T_0)/(T_M - T_0)$	dimensionless temperature
$T_p^* = (T_p - T_0)/(T_M - T_0)$	dimensionless peak temperature
$q^* = Aq / r_B \lambda (T_M - T_0)$	dimensionless beam power
$v^* = v r_B / a$	dimensionless beam velocity
$t^* = t / t_0$	dimensionless time
$t_p^* = t_p / t_0$	dimensionless time to peak temperature
$t_0 = r_B^2 / 4a$	heat flow time constant (s)
$x^* = x / r_B$	dimensionless Cartesian coordinate x
$y^* = y / r_B$	dimensionless Cartesian coordinate y

$z^* = z / r_B$	dimensionless Cartesian coordinate z
$z_0^* = z_0 / r_B$	characteristic length
$q_R^* = Aq / w\lambda(T_M - T_0)$	dimensionless beam power of non-Gaussian beam
$v_R^* = vw / a$	dimensionless velocity of non-Gaussian beam

Abbreviations

HAZ Heat-Affected Zone

LSA Laser Surface Alloying

Chapter 1

Introduction

The laser has arguably become one of the most versatile and valuable tools to many industries. Aerospace, automotive, and electronic industries, to name a few, rely heavily on the laser (Charschan 93). Welding, drilling, surface modification, cutting, and marking have become the laser's mainstays in material processing (Ready 97). These processes all have a common requirement from the laser, that of maintaining a desired level and spatial distribution of the laser's energy incident on the material. The requirement can be met with proper focusing of the laser beam onto material, which is normally not a problem when material dimensions are precisely known within a small tolerance. In applications where dimensions vary significantly from piece to piece and laser material processing is needed, working distances can deviate from the ideal focus distance.

The effect of this deviation on processing quality must be understood in order to correct it. While changes in laser energy densities resulting from improper focusing have been well studied for Gaussian sources (Cline and Anthony 77, Lax 77), more complex beam profiles can present problems in calculating these changes. In many cases these problems are solved numerically, but when moving non-Gaussian heat sources are taken into account the numerical solutions become more difficult. While these problems can be solved numerically by updating initial conditions at each new beam position in time based on the beam's previous transient temperature field solution, this can require long computer processing times. In addition, the information gained from such calculations can be more than needed for single track predictions of melt zone depth and heat affected zone (HAZ) depth for a moving non-Gaussian heat source. For the main focus of this research, which is Laser Surface Alloying (LSA), these measurements will be the scope of the properties that will be considered as an indicator of final processing quality.

Surface modifications such as laser hardening and LSA are known methods for changing a material's surface properties in order to improve them (Charschan 93). In the case of LSA, corrosion and wear resistant surface properties can be achieved on base metals such as aluminum and steel. The LSA process used for this research begins with application of a precursor layer, which consists of the powdered metals to be added along with a binding agent, on to the base metal surface. After the precursor has dried and stabilized the powdered metals within the binding agent, the new surface components and a portion of the base metal are melted by the laser and mixed primarily by surface tension driven convection. The depth of the alloyed layer is primarily controlled by laser parameters such as beam energy density, total absorbed beam power, and beam velocity. As the beam energy density value becomes unacceptable through improper beam focusing, the result can be undesirable melt depth and track geometry, along with process inefficiency if more beam power is incorrectly applied to correct shallow melt depth. For the LSA process, maximum aerial coverage per processing track is needed in order to minimize the number of tracks and thus processing times. Using a laser beam profile with a large width and a relatively narrow length increases the aerial coverage in this case. This line beam profile can present problems in determining temperature distributions as alluded to earlier. If temperature distributions can be accurately predicted, the extent of negative defocusing effects on final LSA quality can be quantified before processing, thus providing a range of acceptable focus distances. In order to keep the focus distance within this range, techniques must be devised to insure that the optics are held within these distances from the workpiece. Workpieces with known dimensional tolerances smaller than the optimum processing focus range usually present no problems in maintaining proper focusing because the motion system can be programmed to accurately follow the surface geometry, so items that have relatively large dimensional tolerances outside the optimum processing focus range will be considered as examples of processing difficulties which need to be addressed. These pieces might be encountered when processing existing in-use structural assemblies for corrosion resistance or processing wear prone items for rebuild or repair. Due to the unknown variations of geometry from piece to piece, it would be impractical or impossible to follow the geometry without a form of a distance feedback system. The idea that is considered here within is an automatic focus control system.

The ability to measure distances from the workpiece in-process can provide the necessary feedback to correct focus distances that are outside an acceptable range. A simple mechanical follower that is allowed to ride along the workpiece surface could accomplish this. One problem with this approach is that the follower is a contact device. This is not ideal for the LSA application in this instance because the precursor that is applied before processing may be disturbed by contact. In other laser processing applications, a contact device introduces the possibility of wear, contamination, and low resolution for sharp changes in workpiece geometry. Alternately, a non-contact measuring device such as a laser triangulation distance sensor can be used. These devices provide quick sampling rates and high resolution, but extra equipment needed for the measurement system can be expensive to initially install and also to maintain over time. In order to justify any distance feedback system's use, the acceptable range of focus distance must be shown to be smaller than the intended application's geometrical tolerances. Also, in considering a control system, limitations on the dynamic response of the focus related motion system need to be considered. The intended purpose of this research is to provide evidence that in general cases the use of an automatic focus correction system is warranted and feasible for laser processing and LSA in particular.

A basic outline of the steps needed for the investigation of final processing properties will begin with an experimental approach. In this approach, material samples were subjected to the LSA process at various distances from the optimum processing focus distance. Laser beam velocity, precursor thickness, material type, and laser power were held constant for all trials. Laser beam profile measurements were also conducted for the various trials. After undergoing the LSA process, each set of tracks corresponding to the different trials were analyzed. Through visual microscopy analysis of the melt and heat affected zones, measurements of zone boundaries were conducted. Next, the experimental data were analyzed to determine the extent of an automatic focus control system's theoretical performance based on existing processing equipment specifications. Finally, a theoretical temperature distribution simulation technique will be used to determine the positions of peak processing temperatures. This approach will include an analytical line beam heat source approximation of moving source which will also include a superposition of multiple Gaussian heat sources in order to simulate a non-Gaussian line beam profile absorbed at the surface. By analytically approximating temperature distributions, the major physical events governing heat transfer during LSA can be studied without extensive numerical calculations. Since the approach allows for a non-Gaussian beam profile, more relevant and realistic conditions can be modeled, and experimental beam profile measurement information was used in the modeling stage as the basis in the construction of the non-Gaussian beam profile simulation. Due to the investigation of temperature distributions in a cross-sectional plane of the LSA track perpendicular to the beam velocity direction only, a line beam approximation has been considered. By scrutinizing the data from the theoretical and experimental sections of the research, the extent to which deviation from the optimum processing focus distance affects final processing properties was determined.

Chapter 2

Background

In this chapter, the key characteristics of laser material processing and LSA associated with laser beam defocusing effects are discussed. Background information such as descriptions of laser beam power density levels and laser beam profiles associated with laser material processing and LSA were covered. Additional information includes a description of the temperature distribution simulation technique used, the basic principles used to construct the simulation technique, and limitations and assumptions of the technique.

2.1 Laser Material Processing

The use of the laser has found its way into many applications. Since its invention in 1960, the unique properties of the light produced by the laser have proven useful for a range of devices and processes. One application that has been widely adopted because of these properties is material processing. At the present, the laser has widespread use in the areas of the aerospace industry, electronics production, and the automobile industry (Charschan 93). The production of nearly monochromatic light by the laser allows the selection of a laser light wavelength that is matched to a particular material's peak absorption wavelength. Similarly, a transfer medium, such as a fiber optic, with a peak absorption wavelength differing from that of the laser's wavelength can be used to avoid excessive energy loss or overheating. Also, because laser light is highly collimated, it can be focused into a very small beam spot, which provides large laser power density levels. These power density levels make the laser ideally suited for the hardening, melting, or vaporization of materials. In order for these processes to be precisely controlled, the power density must be maintained at the desired value and distribution along with proper regulation of other processing parameters such as processing velocity and surface preparation. The processing velocity and surface preparation can usually be well controlled through the mechanical movement of the focusing optics and thorough preprocessing preparation of the workpiece respectively. Furthermore, if the laser power output does not fluctuate excessively, the beam power density magnitude and distribution can be maintained during processing if proper focusing of the laser beam spot is held constant.

In the case of material processing, the movement of the laser beam spot over the material surface during processing is usually necessary. If the material is not flat, or planar, there will be the need to translate the focusing optics up or down relative to the material surface in order to maintain proper laser beam focusing. As long as the spatial relationship between the focusing optics and the material is known, necessary movements can be programmed and executed as the beam spot is translated across the material surface. If, in general, this spatial relationship is not known before processing, the relationship must be monitored and corrected during processing if it is outside of a selected range. This range is based on the extent the beam power density profile changes during a change in the displacement of the focusing optics from the material surface and how much fluctuation in the beam power density profile is acceptable for a particular application.

In order to understand these ideas, the behavior of the laser beam profile at the material surface during focus relationship changes and temperature distributions in the material resulting from these laser beam profiles must be investigated. This investigation is the goal of this research and could be accomplished through purely theoretical calculations using ideas from geometric optical theory and analytical or numerical temperature distribution solutions for moving heat sources. This approach can require extensive calculations or computer run-time and provide unneeded information such as in full numerical temperature distribution solutions through time. Analytical temperature distribution solutions can also be limited to simplified point, line, or Gaussian laser beam characteristics. However, if the laser application being studied has more complicated beam characteristics, a more efficient approach is a combination of experimental studies and analytical approximations.

2.2 Description of LSA

Laser surface modification is performed by heating or melting a thin layer of material at the surface of the workpiece with a laser in order to modify its surface properties (Ready 97). The main forms of laser surface modification are surface hardening, alloying, glazing, and cladding with these techniques having many characteristics in common (Grigoryants 94). Laser surface hardening is the process of using a laser to heat and change the microstructure of a thin layer of material at the surface in order to modify the layer's hardness. This change in microstructure usually consists of transformation hardening through austenite formation of the surface of materials such as carbon steels, tool steels, and cast irons to depths of up to 2.1 mm for

AISI 4340 steel using a 3.6 kW CO_2 laser beam at a power density of 1.48 kW/cm^2 and a translation rate of 1.27 cm/s (Charschan 93). Laser glazing is a similar process to laser surface hardening except melting of the surface occurs. This procedure produces a glassy, non-crystalline surface, which can be resistant to corrosion and has very small grain sizes in the surface layer that is melted (Ready 97). Laser cladding involves metallurgically bonding an overlay material to surface of a base material by melting just enough base material to perform the bond. In this process costly material can be bonded on to an inexpensive base material thus providing the surface properties of the expensive overlay to the base material (Ready 97).

LSA combines the basic idea of laser cladding with greater mixing of the base material with the elements to be added. Some examples of the elements added are silicon, boron, carbon, titanium, and chromium (Grigoryants 94). A powder mixture called precursor containing the substances to be alloyed with the base material's surface that is either dry or mixed with a binding agent is applied to the surface before LSA in the case of the bound powder mixture. The dry powder mixture can be applied before LSA or during LSA such as with a powder jet. In the case of the powder mixture and binder, the slurry is allowed to dry before processing, which stabilizes the powder mixture during material handling. Usually a CO_2 or Nd:YAG laser operating at multi-kilowatt levels is then used to alloy the powder mixture into varying depths of the base material depending on precursor thickness. The laser beam is scanned over the surface in a raster pattern creating processed strips called tracks. Each track slightly overlaps the previous track to insure complete coverage as indicated in Figure 2.1. This process is continued until the

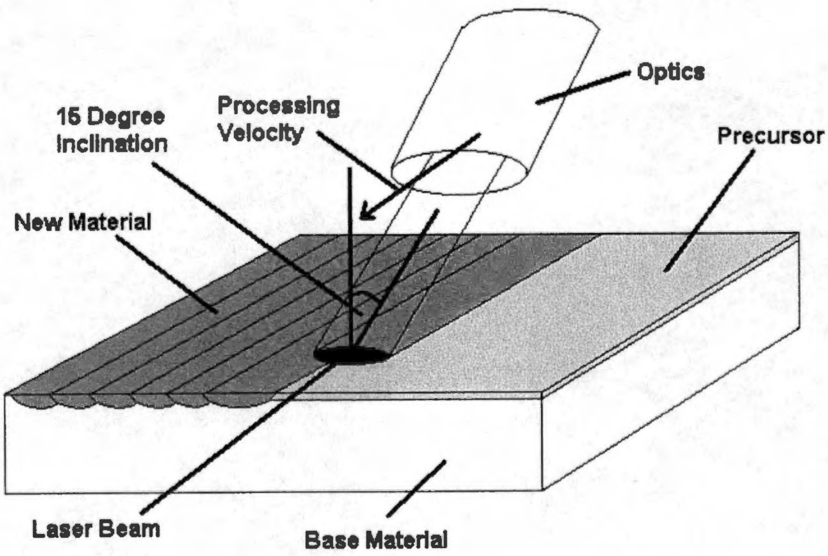

Figure 2.1 Layout of LSA Process

desire area of the workpiece is covered. Uses for LSA include corrosion prevention and wear resistance.

2.3 LSA Laser Beam Power Density Levels

Laser beam energy transfer into the material during laser surface modification techniques is usually small when compared to other laser processing techniques such as welding, cutting, and drilling. This shallow heat penetration depth is accomplished through the use of lower power density levels than that of welding, cutting, and drilling. Typical power densities used for laser surface treatments are around 10^3 to 10^4 W/cm^2 as opposed to power densities greater than 10^5 W/cm^2 for welding, cutting, and drilling (Charschan 93). Unlike other laser material processing fields such as laser welding, cutting, and drilling where beam power densities are high enough to allow for material vaporization, beam power densities for laser surface modification at the material surface are not sufficient to reach the target material vaporization regime.

Beam power density levels used in laser surface treatment must be precisely controlled because heat penetration depth and thus final processing characteristics for given material are dependent on the power density levels assuming other processing conditions are maintained such as absorptivity and beam velocity. The melt depth can be approximated by

$$d_m = \frac{A}{v\rho[C(T_m - T_0) + L_f]} \frac{P}{b} \qquad (2.1)$$

where v is the beam velocity, P is the beam power, A is the surface absorptivity, L_f is the latent heat of fusion, T_m is the melt temperature, T_0 is the initial temperature, and b is the diameter of the beam spot, and is directly related to the beam power over the beam diameter or area which is the power density (Charschan 93). In LSA heat penetration depth and melt depth also dictate surface alloying mixing percentages of base material and precursor materials. A decrease in beam power density levels can result in unacceptable surface alloying due to insufficient transfer of laser energy to the workpiece. Insufficient mixing of precursor materials with the base metal or no melting of the base metal result if insufficient transfer of laser beam energy to the workpiece occurs. An increase in power density levels can lead to over-mixing of precursor materials with the base metal and a deeper than expected alloyed layer. If these variations in beam power density levels from the desired level take place, the ideal operating conditions are not met and final processing quality suffers. The extent of the effect that variations in beam power density due to beam defocusing have on final processing quality is investigated in this research.

2.4 LSA Laser Beam Profiles

Laser surface treatment techniques for the most part involve processing a surface track by track in a raster pattern. In order to reduce the number of tracks and processing time needed, the laser beam spot must cover as much area as possible while maintaining a sufficient power density level. It is therefore desirable to use a laser beam profile that has a large width across the processing track as compared to the length along beam travel for surface treatment processes. This is opposed to most other forms of laser materials processing such as welding, cutting, or drilling. In these cases, a laser beam profile with a circular distribution is generally used. Spherical lenses and mirrors are generally used for the focusing optics because the basic laser beam profile output from the laser is sufficient for these applications. There is no need to modify the general beam profile with the delivery optics. LSA and other surface treatment processes, however, do benefit from a laser beam profile modified from that of the profile output directly by the laser to that of a profile with a larger width described earlier. This modification can be accomplished through the use a beam integrator or the focusing optics. A beam integrator usually consists of a multifaceted mirror, which overlaps individual images to create a square beam pattern with a relatively uniform power distribution (Charschan 93). Focusing optics which can create a wide beam can be comprised of two plano-cylindrical lenses rotated 90° relative to each other in the focusing optics assembly. Plano-cylindrical lenses are used refract light in one dimension only, and due to this property, can be used to transform a circular source of light in into a rectangular or oblong source. The effect of the first cylindrical lens in the assembly is to refract the circular beam profile into a diverging line profile. By placing the second plano-cylindrical lens as a converging lens and rotating its refraction axis 90° relative to the first lens, the diverging line profile produced by the first lens is refracted into a beam profile with a relatively large width as compared to its length at certain focus distances.

2.5 Basic Principles of the Temperature Simulation Technique

As a laser beam irradiates an area on the surface of a material, that area absorbs a portion of the laser's energy through radiation heat transfer and heating of the area begins. If the laser energy is not sufficient to vaporize the material, the radiation heat transfer can be said to occur strictly at the material surface since laser radiation penetration is generally limited to range of 0.1 to 1.0 μm (Grigoryants 94). The transmission of the heat throughout the material is primarily performed by conduction and, in the melted region, surface tension driven convection. Conduction of heat dominates the transfer of heat until the laser-induced temperature rise is sufficient to melt the material. Also, melting is limited to a shallow layer at the surface for those power densities found in the field of laser surface treatment, and thus the heat transmission can be approximated by heat conduction theory. Any method of solving a heat conduction problem must begin with the fundamental expressions predicting heat flow in a substance. The heat conduction rate equation for a three-dimensional solid is given by

$$\rho C \frac{\partial T}{\partial t} = \frac{\partial}{\partial x}\left(\lambda \frac{\partial T}{\partial x}\right) + \frac{\partial}{\partial y}\left(\lambda \frac{\partial T}{\partial y}\right) + \frac{\partial}{\partial z}\left(\lambda \frac{\partial T}{\partial z}\right) + q'''(x,y,z,t) \tag{2.2}$$

where q''' is the volumetric heat source, ρ is the material's density, C is the specific heat, and λ is the thermal conductivity. If the thermal properties are time, space, and temperature independent, then this equation reduces to

$$\nabla^2 T - \frac{1}{a}\frac{dT}{dt} + \frac{q'''}{\lambda} = 0, \quad a = \frac{\lambda}{\rho C} \tag{2.3}$$

where a is thermal diffusivity. Solutions to this rate equation for different source configurations related to laser processing have been performed and are well documented. The temperature field solution found using a moving point source for the heat generation term in the rate equation by Rosenthal (46) is

$$T - T_0 = \frac{Aq}{2\pi r} \exp - \left\{ \frac{v}{2a}(x + r) \right\} \tag{2.4}$$

where A is the surface absorptivity, q is the beam power, v is beam velocity, a is the thermal diffusivity, r is the radial distance to point of temperature rise, and x is the beam position. Further work with point source solutions has also been performed by Carslaw and Jaeger (59). Cline and Anthony (77) extended these point source solutions to include a Gaussian beam shape by integrating point sources over the area of the beam. The expression for the temperature field,

$$\begin{aligned} T &= \int_{-\infty}^{t} \int_{-\infty}^{\infty} \int_{-\infty}^{\infty} \int_{-\infty}^{\infty} (q / C)(x'y'z't') * G(x'y'z't' \mid xyzt) dz'dy'dz'dt' \\ G &= \frac{\exp[-r^2 \{4a(t - t')\}^{-1}]}{4[\pi a(t - t')]^{3/2}}; r^2 = (x - x')^2 + (y - y')^2 + (z - z')^2 \end{aligned} \tag{2.5}$$

is quite complex involving multiple integrals and a Green's function. Lax (77) and Sanders (84) have completed similar work. Although these solutions are thorough, numerical techniques must be used to evaluate them. Furthermore, results are often more than needed for the peak temperature field solutions, which can be used to approximate final processing characteristics for laser surface processing techniques.

Bass (83) developed another approach of approximating peak temperatures of materials heated by a moving laser beam. In this approach, limits are taken on temperature field equations for various beam geometries to provide analytical results. Ashby and Easterling (84) continued this technique and developed an expression that approximates the complete temperature distribution. By using a form of the Gaussian line source developed by Rykalin et al. (78),

$$T - T_0 = \frac{Aq}{2\pi\lambda v[t(t+t_0)]^{1/2}} \exp - \frac{1}{4a}\left[\frac{(z+z_0)^2}{t} + \frac{y^2}{(t+t_0)}\right], \quad t_0 = \frac{r_B^2}{4a} \tag{2.6}$$

Ashby and Easterling introduce the term, z_0, which limits the surface temperature to finite values by offsetting the heat source a distance of z_0 above the true surface. They evaluate z_0, the characteristic length, in two limits. These limits are for heating times much less than and much greater than the heat transfer time t_0 and are equivalent to the near field and far field solutions respectively. The characteristic length z_0 is then determined separately in each case. Shercliff and Ashby (91) expanded this technique by describing a method for determining z_0 that is adequate for the entire temperature field, and this is the temperature distribution approximation used in this research. This approach is discussed in detail in the Chapter 4.

2.6 Description of LSA Temperature Distribution Simulations

Due to the non-Gaussian shape of the beam used in this case for LSA, traditional analytical approaches to the prediction of temperature distributions cannot be directly applied. An approximation of the temperature distribution must be made. In this investigation a moving non-Gaussian laser beam profile is approximated by a stationary beam constructed of the superposition of multiple Gaussian beams. The theory is based on the work of Shercliff and Ashby (91). They have developed a method of predicting approximate temperature distributions for a moving arbitrary laser beam profile used in laser hardening. The basic procedure utilized by Shercliff and Ashby involves combining multiple Gaussian beams with various power levels in a spatial orientation so that the integrated profile closely matches that of the general laser beam. The power levels and location of the Gaussian beams are adjusted to resemble the beam power profile of the non-Gaussian beam with the sum of the individual beam power levels equaling the total power of the non-Gaussian beam. The measured beam profiles from the experimental section of this research are constructed in this manner. The temperature contributions from each Gaussian beam are then summed to approximate the temperature distribution from the total non-Gaussian beam (Shercliff and Ashby 91). In this approach, the temperature distribution for the plane located at the mid-point of the beam's length parallel to a cross-section normal to the direction of beam travel of a processed track at a point in time is given. If the time to reach peak temperatures is used, then the final processing temperature distributions are found thus providing the final processing characteristics. The expression for the time to reach peak temperature along with all other equations associated with this technique are detailed in the following chapter.

2.7 Limitations and Assumptions of the Temperature Simulation Technique

As this technique is an approximation there are some limitations and assumptions. Shercliff and Ashby outline their explicit assumptions in their article. There are also some assumptions imposed in association with the research involving LSA. Shercliff and Ashby (91) state that it is assumed that the surface absorptivity, thermal conductivity, and diffusivity are all constant along with the assumption that the Gaussian beam radius is measured from the center to $1/e$ times the peak intensity position and the domain of interest is semi-infinite. They go on to state that the heat of fusion is assumed negligible compared to other terms in the heat flow equations. Implicit assumptions imposed for this research that follow closely to the above are that there are no convective or radiative losses relative to the major terms in the heat flow equations at the boundaries. The initial temperature of the material is also assumed to be constant spatially throughout the material.

Limitations of this technique include the fact that temperature distributions are predicted for single processed tracks only since there cannot exist a non-uniform initial temperature distribution. Furthermore, Shercliff and Ashby state a beam profile geometry limitation involving the experimental beam peak temperature calculation that is discussed in Chapter 4 in detail.

Chapter 3

Experimental Technique

Experimental research procedures and supporting materials are covered within the chapter. Along with the LSA procedure, this material includes processing material classification, equipment descriptions, beam measurement techniques, and metallurgical analysis procedure.

3.1 Processing Sample Description

Throughout the experimental period of the research, metal samples consisted of AISI-SAE 1010 steel. The steel can be classified as commonly used plain steel with a chemical composition of 0.10 % carbon and 0.42% manganese. The samples (coupons) consisted of 7.62 cm by 15.24 cm by 0.635 cm plates shown in figure 3.1. There was no significance to the geometry other than the coupons are commonly utilized in the research facility. Each coupon was sandblasted to remove surface contaminates and to provide a surface of uniform roughness for the precursor slurry to adhere.

The precursor consisted of a binding agent and component metals to be alloyed into the sample surface. A water-based binding agent was used that allowed metal powders to be applied through air propelled spraying. Once the binding agent had dried, metal components were stabilized on the sample surface. The binding agent would then vaporize during processing. Precursor application thickness was based on previous experiments and quantified during application by the number of coats applied. After the

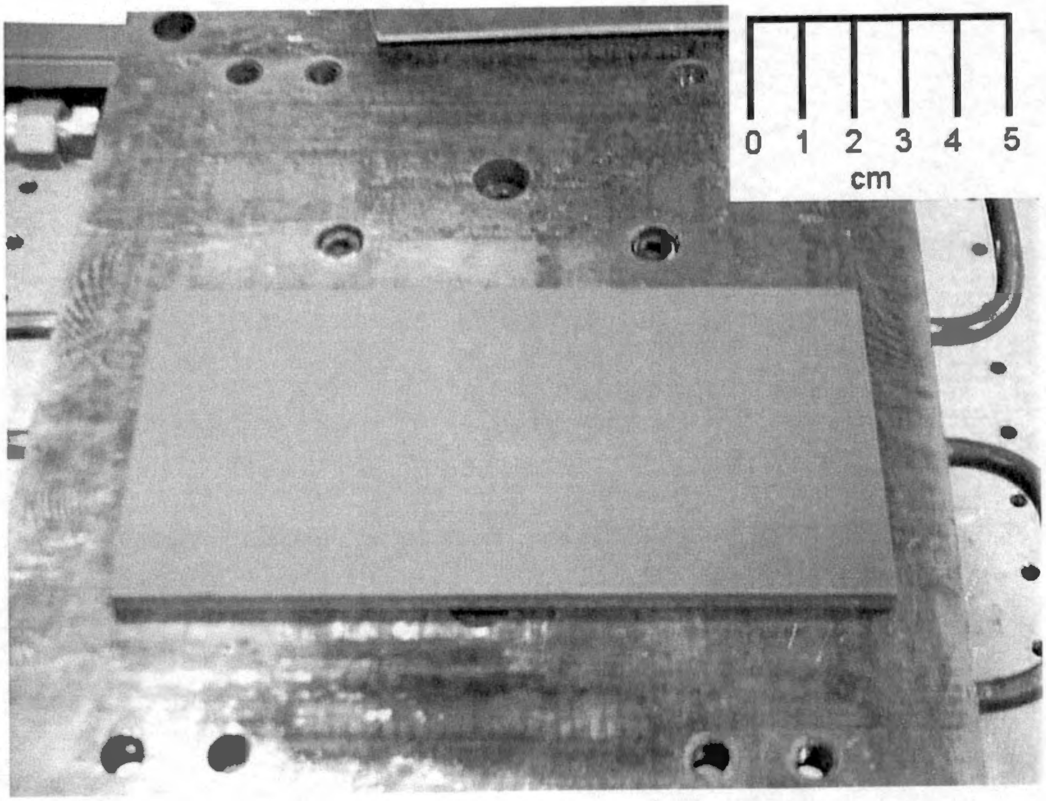

Figure 3.1 View of Material Coupon

precursor slurry had dried and before processing, precursor thickness was measured with a coating thickness gauge and a measuring microscope.

The samples were then divided up into the different cases to be processed. Each case had three processing passes or tracks that were the width of the laser beam spot. The tracks for were separated by 6-8 mm to avoid heat migration into previous tracks.

3.2 Precursor Components

Powdered metals included in the precursor slurry were nickel and chromium. The particle size of the powders was -325 mesh for chromium and less than 1 μm for nickel. Approximately 66% chromium and 34% nickel comprised the precursor by weight. No other substances were used except the facility's own water-based binding agent. The slurry was mixed thoroughly before three coats were applied. The thickness of the three precursor coats totaled 96 μm.

3.3 Laser Processing Equipment

Throughout the length of the processing period, a 3 kW Nd:YAG industrial laser was used and is shown in figure 3.2. The laser operated at a wavelength of 1.06 μm and in multi-mode. A model HLP 3000 laser manufactured by Hobart Incorporated was used and was operated with a continuous duty-cycle. An optical fiber was utilized to deliver the beam to the focusing or end effector optics. These optics consisted of a series of water-cooled cylindrical and spherical lenses. The effector optics were also situated at

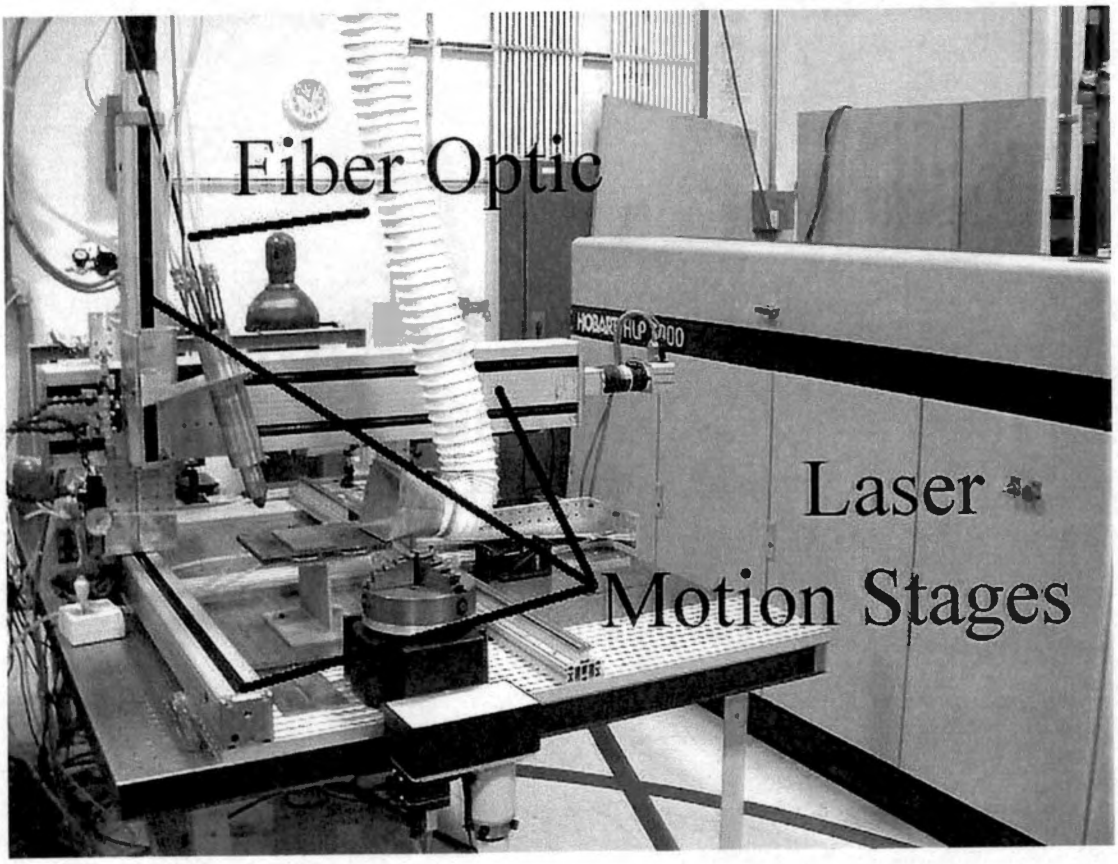

Figure 3.2 Laser Processing Laboratory Layout

15° from normal to the workpiece away from the direction of travel as noted in figure 3.3 to avoid a back reflection into the fiber optic. A compressed air flow was kept in place across the lens closest to the workpiece in order to keep contaminants such as spatter blown free of the lens. Motion of the effector optics was accomplished by a computer controlled motion system.

A motion system consisting of three linear motion stages and one rotary stage was used for the duration of the laser surface processing trials. An Aerotech Unidex 500™ controller card was located in a personal computer. The personal computer provided an interface that was used to program the individual movements of the system and allow for program file and system settings management. The motion stages were manufactured by Techno-Isel Incorporated and featured encoder feedback servos.

3.4 Laser Beam Measurement

The cylindrical lenses used in the effector optics are mounted rotated 90 ° relative to one another in the effector assembly. This configuration is used to produce the line beam employed in these experiments. The BeamScan™ model beam-scanning device was manufactured by Photon Incorporated and was utilized to measure the beam profile at various amount of beam defocus. The scan head was of the rotating type and was interfaced with a personal computer. Parameters such as resolution, measurement averaging, and measurement gain could be adjusted with the personal computer. Beam measurements are listed in table 3.1. The beam aspect ratio, which is defined as the beam length divided by the beam width, is shown for various defocus distances in figure 3.4.

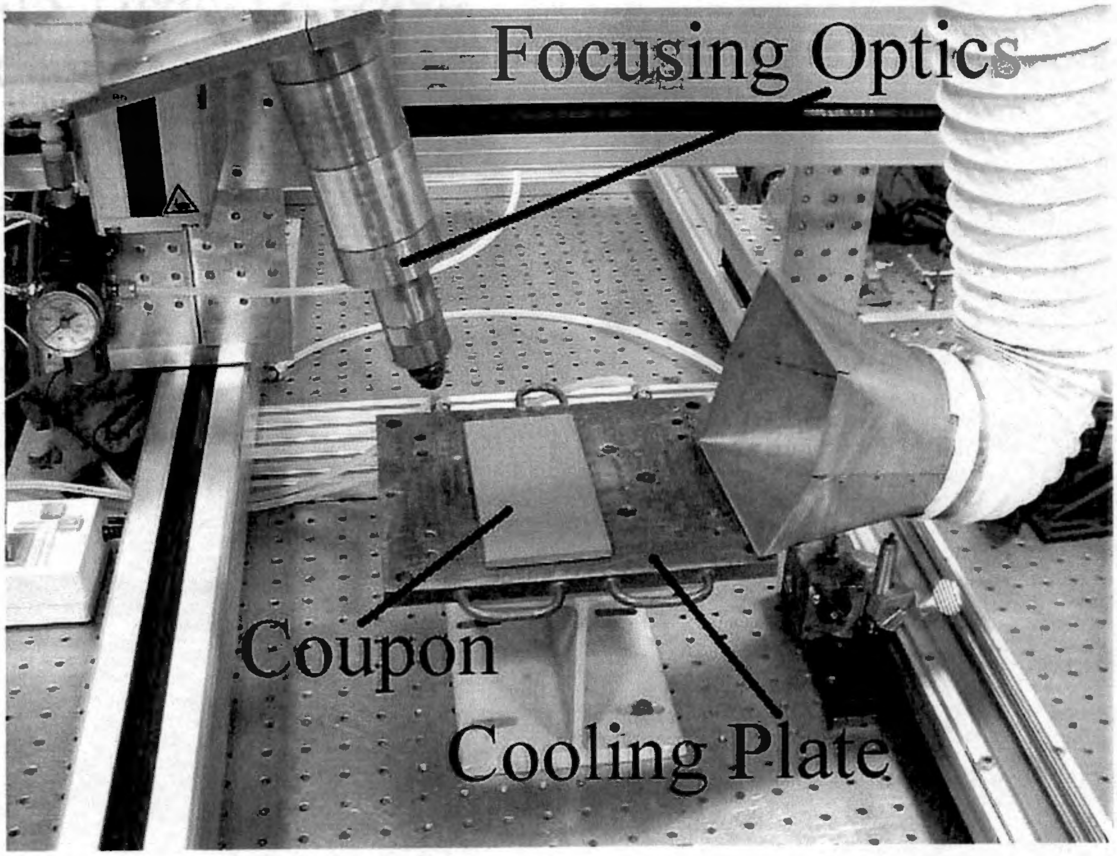

Figure 3.3 Detailed View of Experimental Setup

Table 3.1 Beam Profile Dimensions For Various Focus Distances

Focus Distance Mm	Width µm	Length µm	Area cm^2	Area Ratio	Aspect Ratio (Length/Width)
-0	3203	1017	0.0326	1.00	0.318
-1	3286	1084	0.0356	1.09	0.330
-2	3394	1155	0.0392	1.20	0.340
-3	3514	1233	0.0433	1.33	0.351
-4	3627	1333	0.0483	1.48	0.368
-5	3723	1485	0.0553	1.70	0.399
-6	3854	1593	0.0614	1.88	0.413
-7	3924	1745	0.0685	2.10	0.445
-8	4079	1860	0.0759	2.33	0.456
-9	4194	1991	0.0835	2.56	0.475

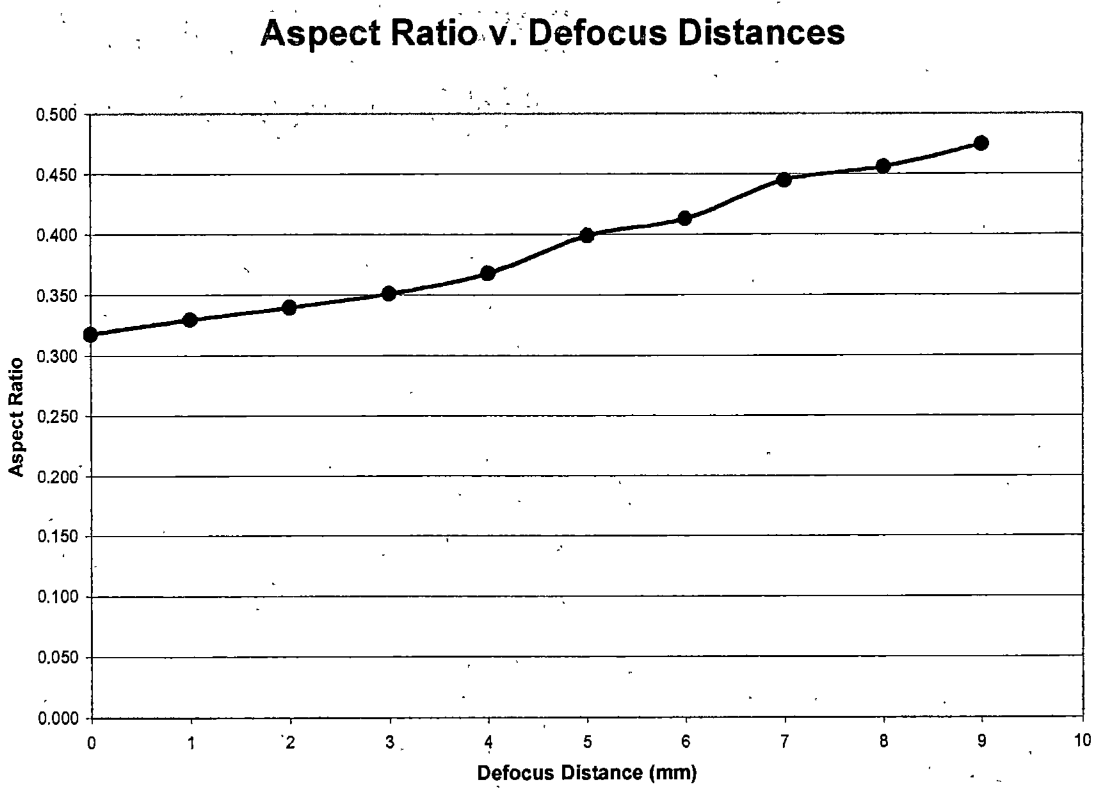

Figure 3.4 Beam Aspect Ratios For Various Defocus Distances

As focus distances grow smaller than the optimum processing focus distance of 115 mm as determined from previous research experience (Schwartz 00), the beam power density decreases while its dimensions grow larger in both width and length. Any large peaks in the beam power profile soften or grow smaller in magnitude, but the basic shape of the beam profile remains constant. The increases in the beam profile dimensions and resulting decrease in beam power density produces a slightly wider and shallower processed track. The same can be said for distances growing larger than optimum processing focus if optimum focus is at the true focus distance. These changes in the laser beam profile occur at the same rate in relation to a change in focus distance whether growing smaller or larger than true focus as given by for a thin lens and a circular beam,

$$\frac{r_1}{r_2} = \frac{d-f}{f} \tag{3.1}$$

where r_1 is the input beam radius, r_2 is the output beam radius, d is the distance from the lens, and f is focal length of the lens (Pedrotti and Pedrotti 93). Since this rate of change is constant, the effect of these beam profile changes resulting from shorter than optimum processing focus distance only are studied in this research. Due to the use of cylindrical lens in the focusing optics during experimental trials, the beam profile becomes elongated in the direction of beam velocity after focus distances grow larger than the true focus distance. For this optics set, information gained from experimental trials conducted at focus distances greater than the true focus distance are unclear because the maximized aerial coverage is negated. Thus, the effect of defocusing for focus distances longer than that of optimum processing focus have not been considered in this research.

3.5 Operating Conditions

Environmental conditions during laser surface processing were kept at room temperature and atmospheric pressure. Laser output power level was held constant for all processing trials with delivered power calculated using optical fiber loss percentages. There was no variation in laser beam traverse speed between trials, so only changes in focus distance were made between processing trials. Shield gases were not used during processing with the workpiece being fastened to a water-cooled copper plate with a thin high heat conducting material placed between the plate and the workpiece. All relevant operating conditions are listed in table 3.2.

3.6 Laser Surface Alloying Procedure

After the sample was mounted to the copper plate, the laser beam was positioned on the sample. The motion controller then executed a program dictating the movements of the laser beam. By processing each new track beside the previous track with a small amount of overlap, the entire surface can be processed. However, in this case single tracks were processed for each trial. Power levels, processing speeds, optimum processing focus distance, and the focus distance range of 115-106 mm were determined from previous processing experience performed at the facility (Schwartz 00). To process, the laser was turned on at the beginning of each track and moved across the

Table 3.2 Experimental Operating Conditions

Laser	Hobart HLP 3000
Laser Power	2000 W
Delivered Laser Power	1850 W
Processing Velocity	5000 mm/min
Tracks Per Trial	3
Coats of Precursor	3
Precursor Composition	Cr 66%, Ni 43% by weight
Optimum Processing Focus Distance	115 mm from optics
Precursor Thickness	96 µm
Material	AISI-SAE 1010 Steel

sample at the selected speed. As energy was added to the material by the laser, the precursor was alloyed into the surface along with a portion of the base metal.

3.7 Metallurgical Analysis

After the steel samples were processed, each had any unprocessed precursor material removed by scrubbing with water and a solvent to aid ease of handling. A portion of each set of tracks, which corresponded to a trial, was sectioned out of the coupon using a wet cut-off saw. This allowed for minimal introduction of additional heat into the processed tracks. The sectioned pieces were mounted into epoxy cylinders using a mounting press and then ground and polished using wet grinding techniques and polishing paste. A 5% Nital etchant, which is 5% nitric acid mixed with ethanol or methanol, was applied to clarify the various layers in the cross-section of the track.

Through the use of visual microscopy, track microstructure was examined. The processed layer and heat-affected zone were visually located in each track. Measurement of the processed layer was accomplished by using a visual length scale with the microscope. The same method was applied to the HAZ, but the actual borders between the zones were estimated using the subtle visual variations in the microstructure. Typically, AISI-SAE 1010 steel does not heat treat very well, however, the high cooling rates of LSA produce a relatively small HAZ that is easily identified as seen in figure 3.5.

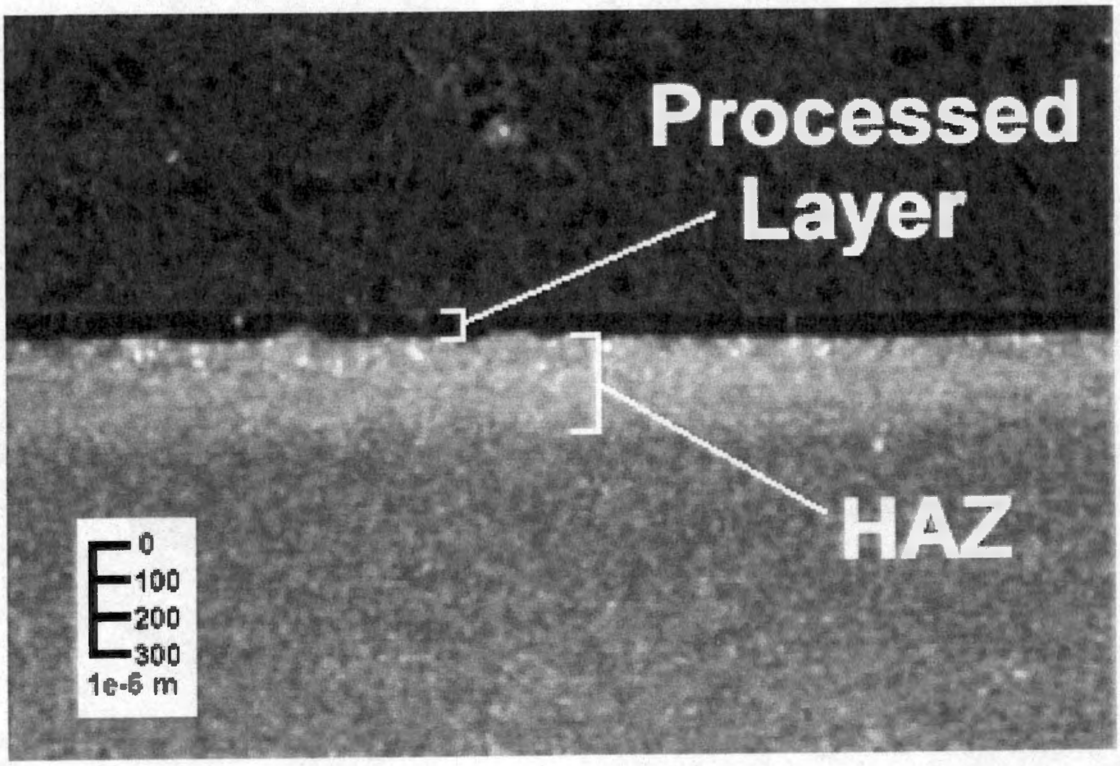

Figure 3.5 Regions of Processed Track Cross-Section

Chapter 4

Temperature Distribution Simulation

The technique of modeling the temperature distribution of the material processed during the LSA experimental trials is discussed. Topics covered include a brief description of the entire simulation technique, the superposition approximation of the laser beam profile, the calculation of the total temperature distribution, the determination of the characteristic length, and the validation of the simulation technique.

4.1 Temperature Distribution Simulation Procedure Description

A stationary laser beam approximation of a moving non-Gaussian laser beam profile is the basis for the temperature distribution simulation. This approach is based on the work of Shercliff and Ashby (91), and uses the superposition of multiple Gaussian sources to simulate a non-Gaussian source. During experimental procedures, laser beam profile data are gathered and used to fit the multiple Gaussian heat sources in order to construct an approximation of the non-Gaussian source. A FORTRAN computer program is written to solve the equations given by Shercliff and Ashby and to aid in data organization. Data manipulation includes finding temperature rise contributions from each Gaussian heat source, summing these contributions, and calculating necessary constants unique to each non-Gaussian heat source by iterative methods. The output data are then plotted and analyzed.

4.2 Non-Gaussian Heat Source Construction Procedure

By investigating the laser beam profile data obtained during the experimental section of this research, it can be noted that the beam profile is generally not Gaussian in shape. In order to utilize the temperature distribution simulation technique based on the work of Shercliff and Ashby, the non-Gaussian laser beam profile must be approximated by combined multiple Gaussian heat sources. This process basically consists of collecting the laser beam profile data taken during the experimental processing trials and adjusting the spatial arrangement and power levels of multiple Gaussian heat sources until their summed intensity profiles best approximate the experimental laser beam profile.

The laser beam profile data collected consists of a three-dimensional visual representation of the intensity profile of the laser beam and sets of values for the centerline intensity profiles for length and width of the beam. Along the beam's length, the dimension parallel with the laser beam velocity, a nearly Gaussian profile was noted. This fact greatly simplified the laser beam profile approximation in that a single Gaussian beam is sufficient to approximate the beam profile along its length. A decision was therefore logically made to use multiple Gaussian heat sources with a beam radius equal to half the experimental laser beam's length. Because of the experimental laser beam's relatively simple profile, five Gaussian heat sources were used to provide a sufficient relative spatial intensity distribution approximation of the laser beam profile. These Gaussian heat sources were located symmetrically along the experimental laser beam's width about the beam profile's centerline. Power levels were then assigned to the Gaussian heat sources and integrated over the entire experimental beam profile in order to approximate the laser beam's intensity profile. The experimental beam profile data for the beam's width and length along with a graphical representation of the Gaussian heat sources and their summation which is the constructed beam's profile are shown in figures 4.1-4.10 for comparison. A three-dimensional representation of the composite constructed beam and Gaussian heat source intensity profiles can be seen in figure 4.11, and a comparison of the intensity profiles of the constructed beam profiles at the beam's width axis for all defocus distances is shown in figure 4.12. Each Gaussian heat source 's beam radius for all trials is shown in table 4.1. The power levels of the Gaussian heat sources were assigned as percentages of the total experimental beam's power and added to equal the beam's total power. These percentages along with the Gaussian heat sources' positions are listed in table 4.2 and for each focus distance. Due to a slight misalignment of lenses in the focusing optics, some asymmetry was noted in trials for -0 mm and -1 mm of defocus, but was negligible in other trials.

Although a simplification was made in the approximation of the experimental laser beam, it should be noted that this approximation procedure was not limited to symmetry along the laser beam's length. The technique developed by Shercliff and Ashby allows for any number of Gaussian heat sources to be used to approximate a non-Gaussian laser beam intensity profile in the dimension parallel to direction of beam velocity. This use of an unlimited number of Gaussian heat sources to approximate a laser beam intensity profile also holds true along the beam width.

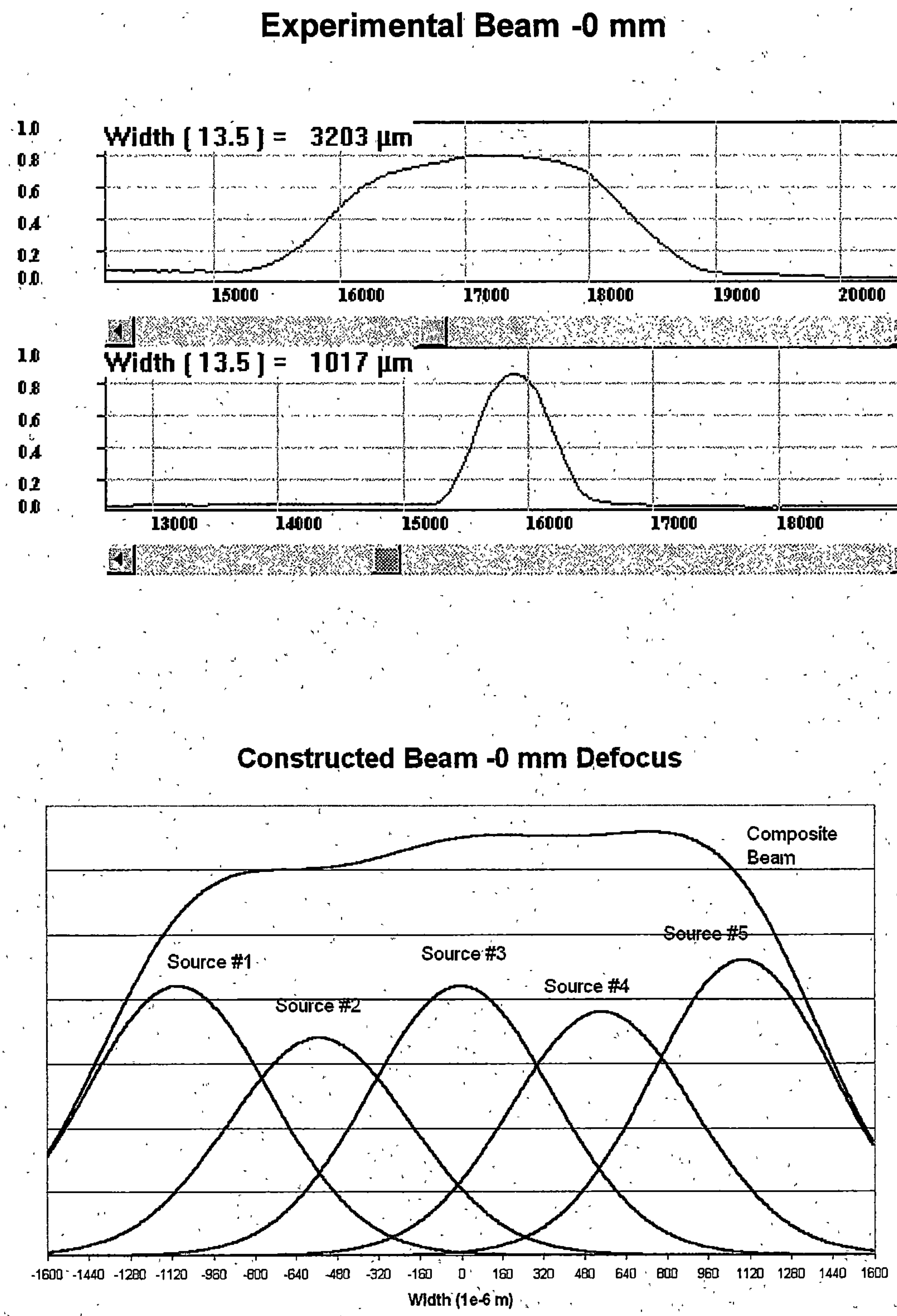

Figure 4.1 Experimental and Constructed Beam Profiles for -0 mm of Defocus

Experimental Beam -1 mm

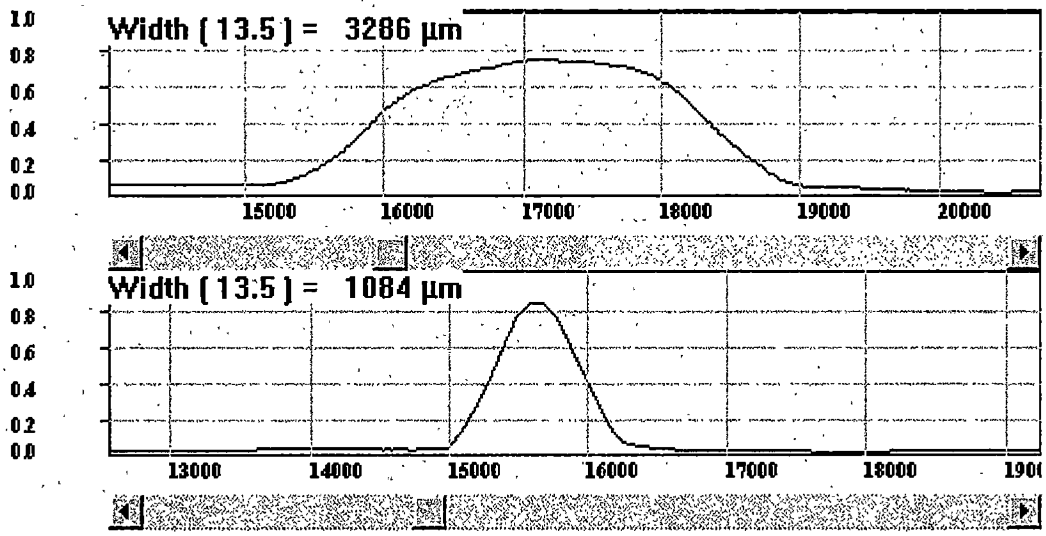

Constructed Beam -1 mm Defocus

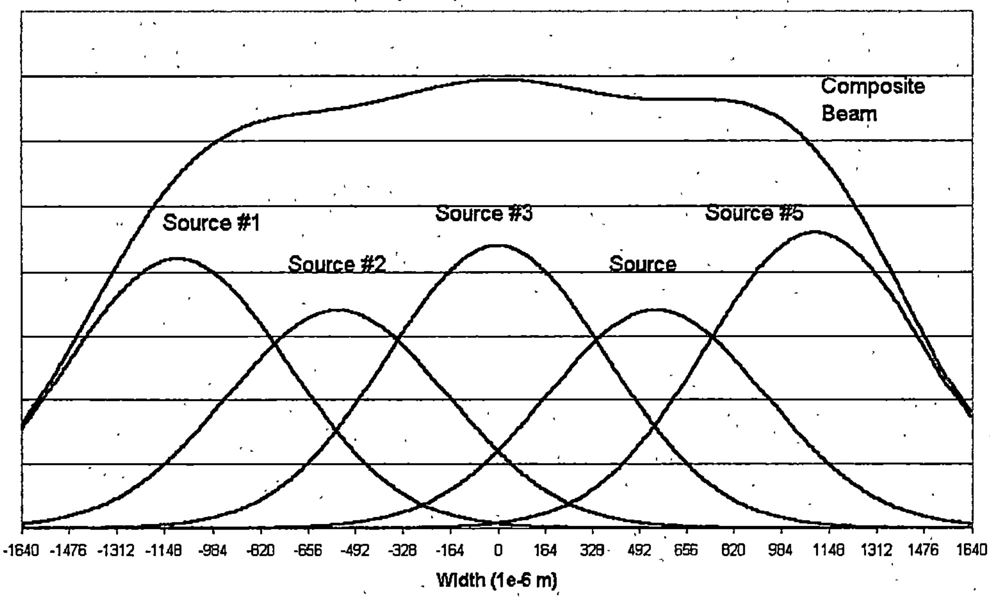

Figure 4.2 Experimental and Constructed Beam Profiles for -1 mm of Defocus

Experimental Beam -2 mm

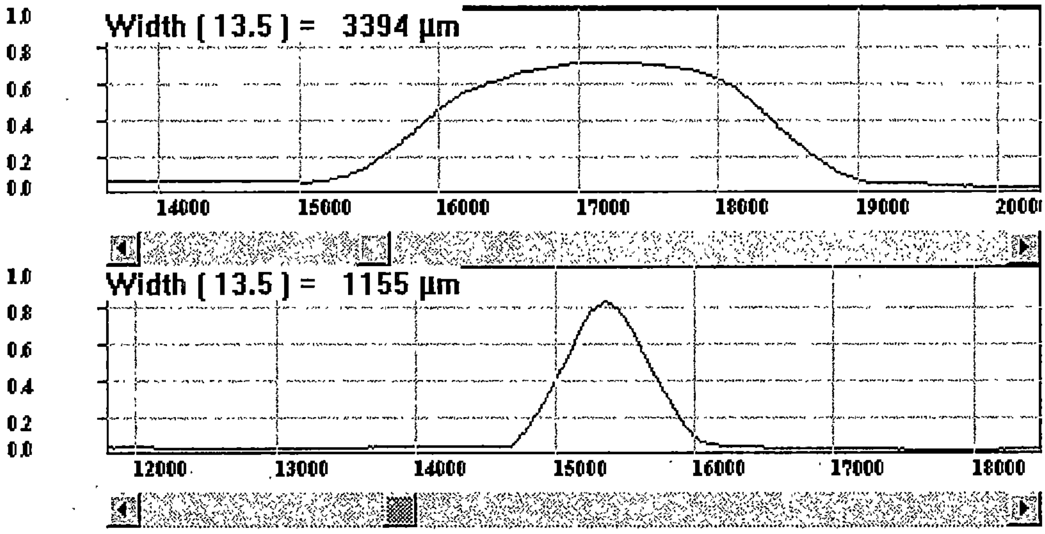

Constructed Beam -2 mm Defocus

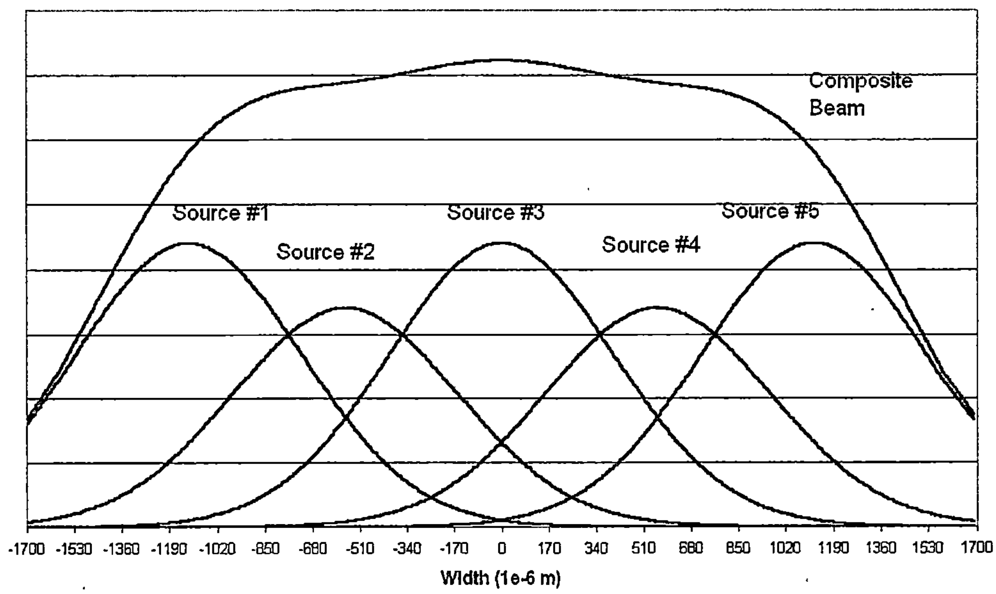

Figure 4.3 Experimental and Constructed Beam Profiles for -2 mm of Defocus

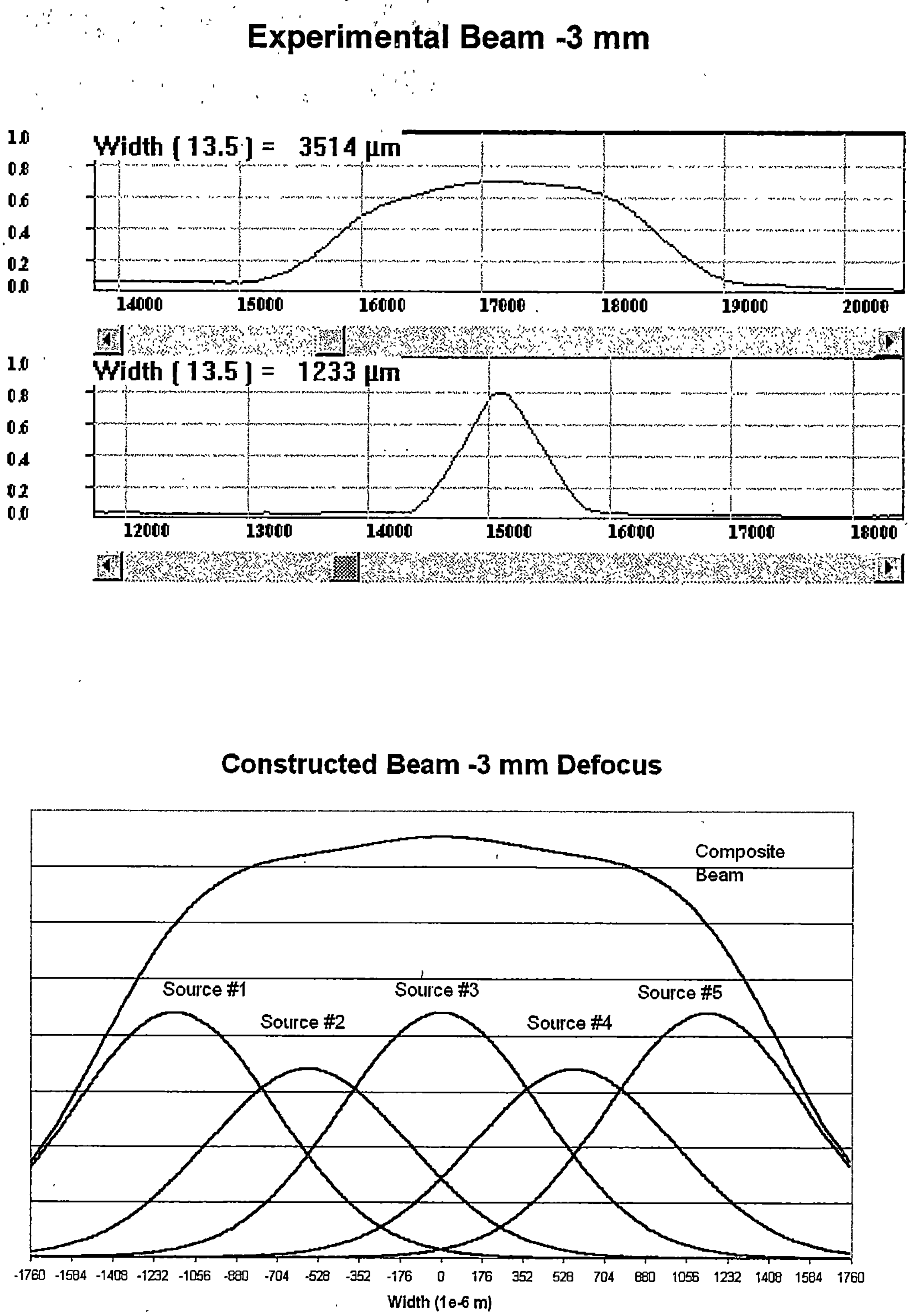

Figure 4.4 Experimental and Constructed Beam Profiles for -3 mm of Defocus

Experimental Beam -4 mm

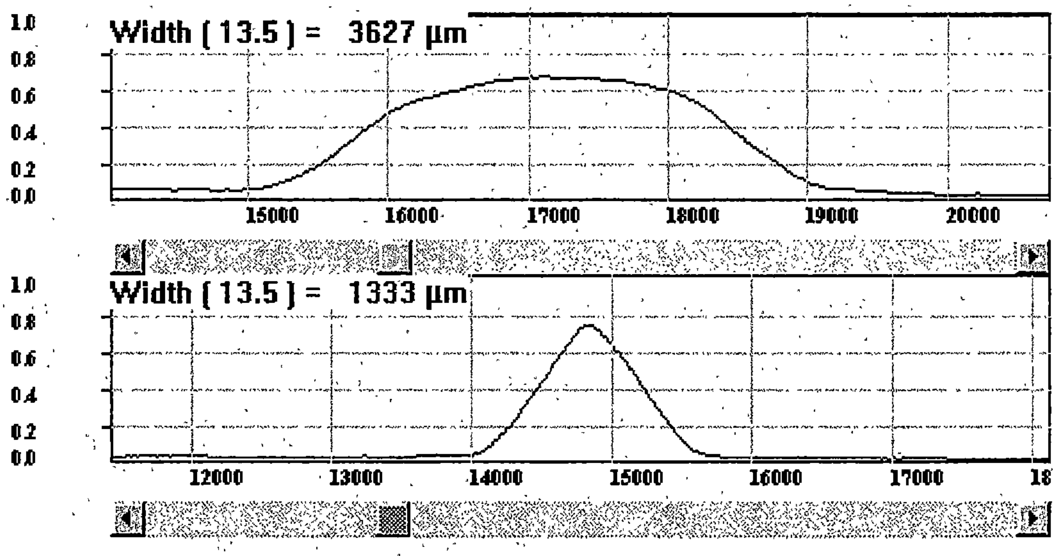

Constructed Beam -4 mm Defocus

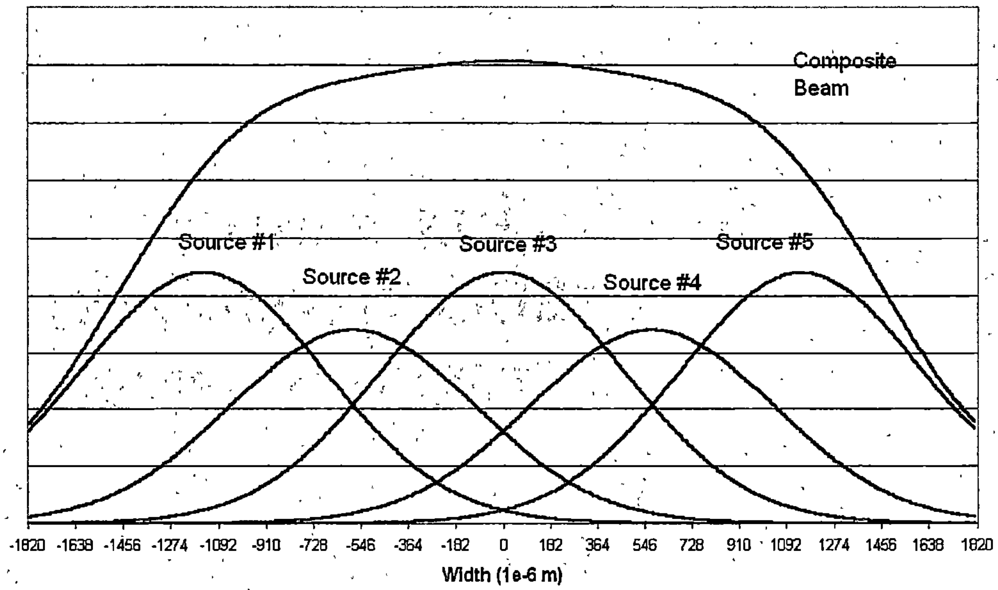

Figure 4.5 Experimental and Constructed Beam Profiles for -4 mm of Defocus

Experimental Beam -5 mm

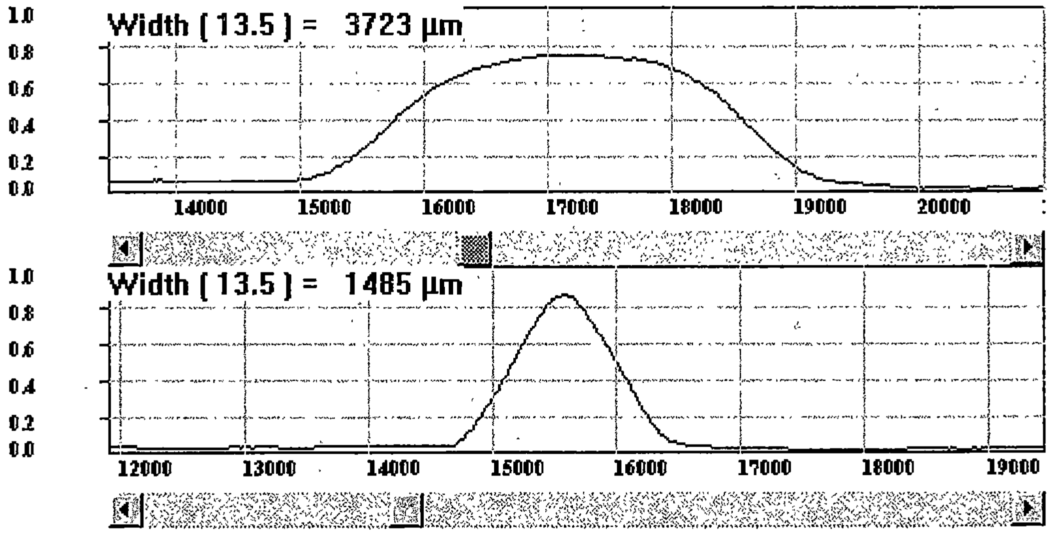

Constructed Beam -5 mm Defocus

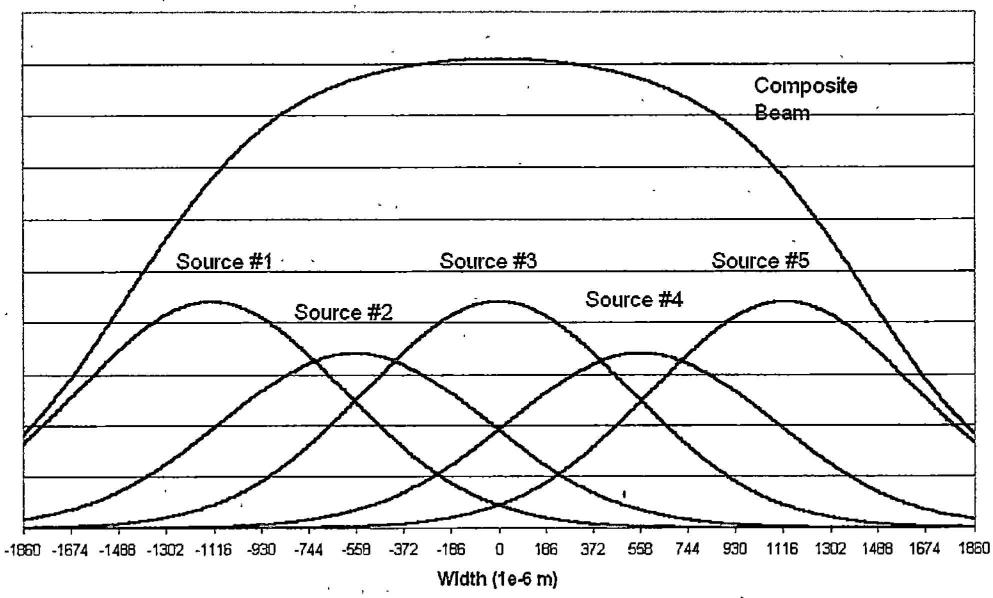

Figure 4.6 Experimental and Constructed Beam Profiles for -5 mm of Defocus

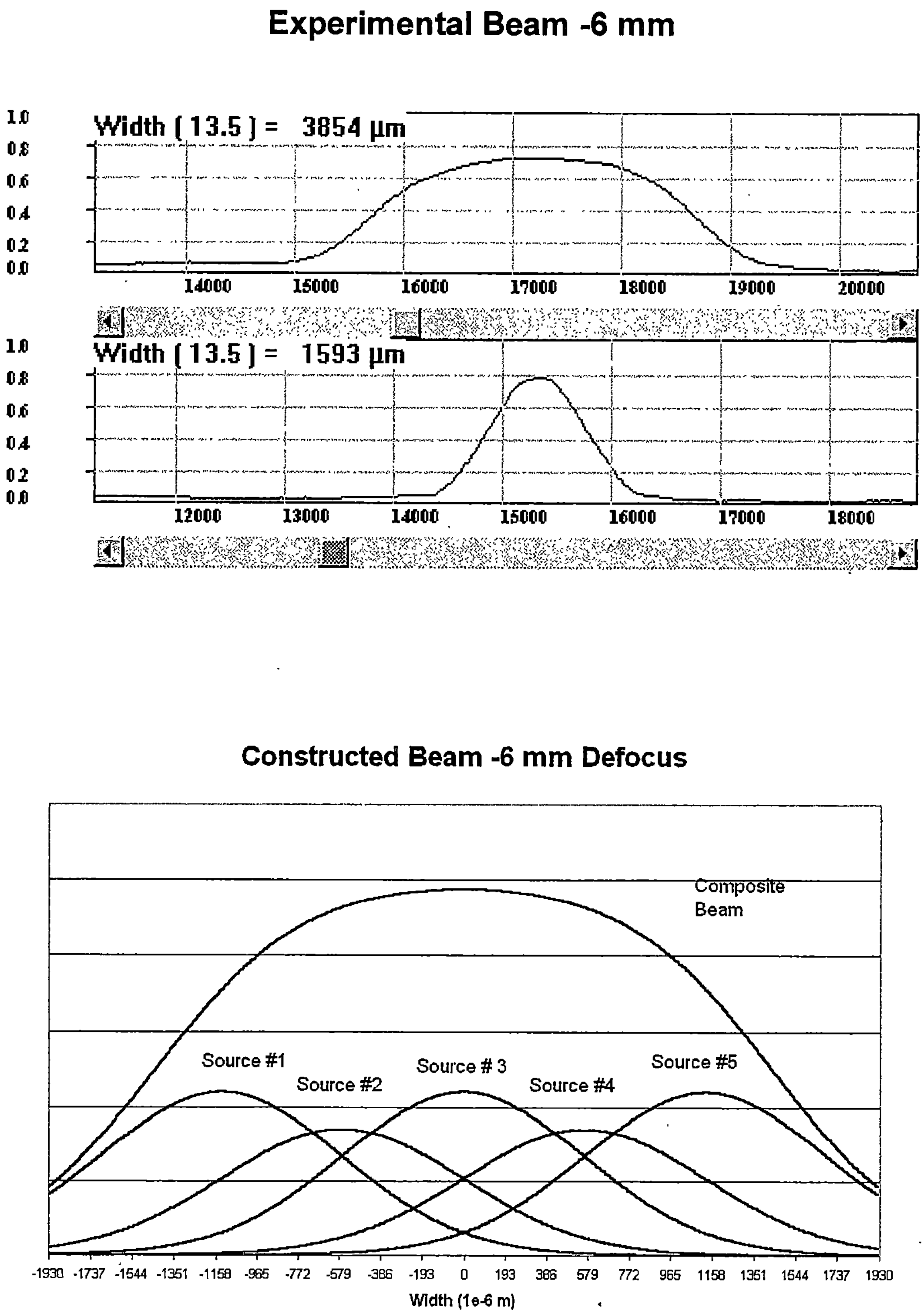

Figure 4.7 Experimental and Constructed Beam Profiles for -6 mm of Defocus

Experimental Beam -7 mm

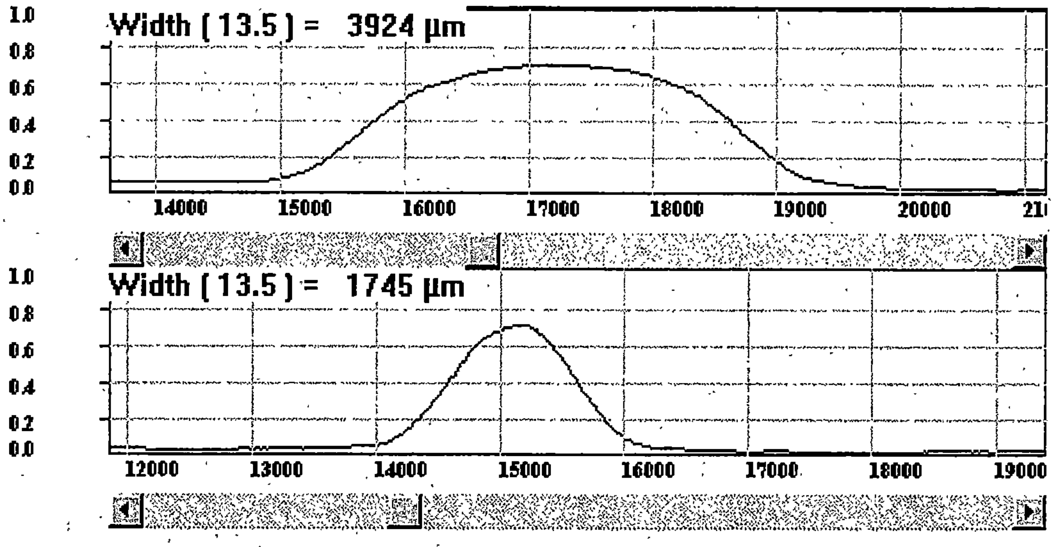

Constructed Beam -7 mm Defocus

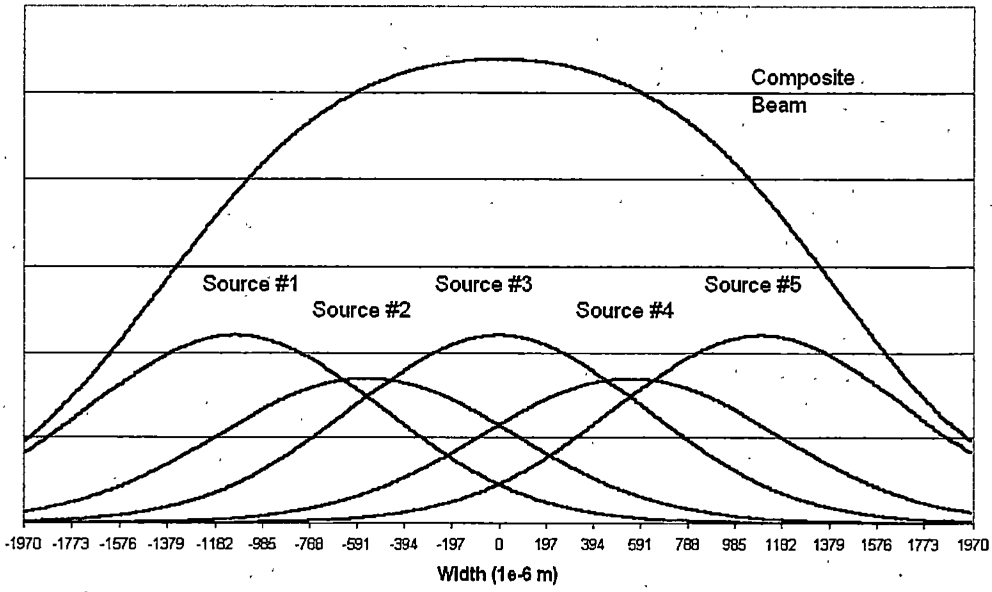

Figure 4.8 Experimental and Constructed Beam Profiles for -7 mm of Defocus

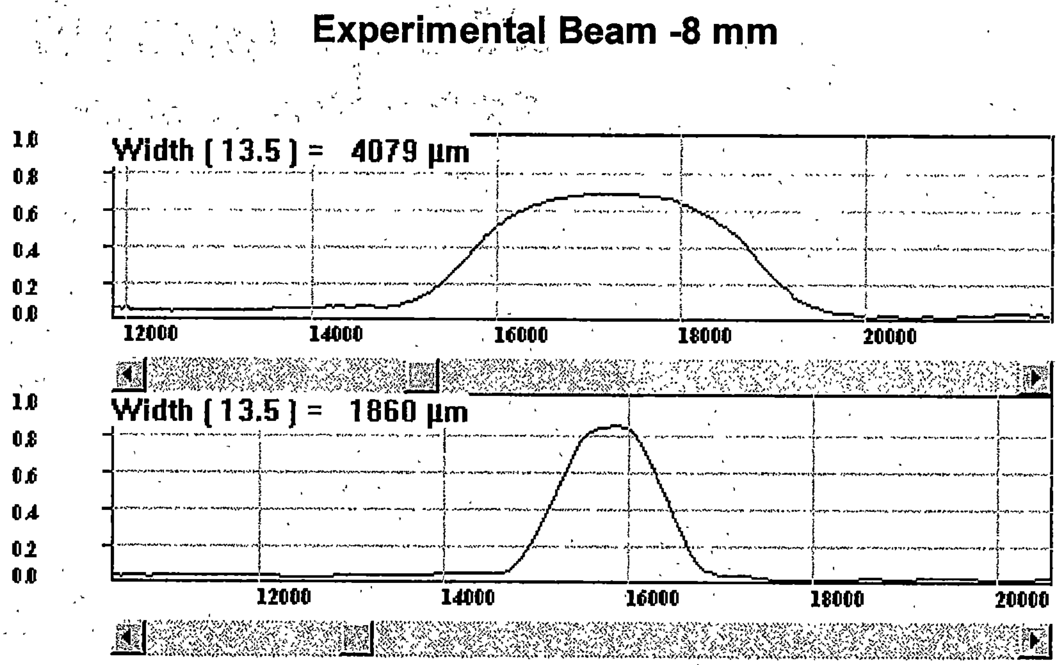

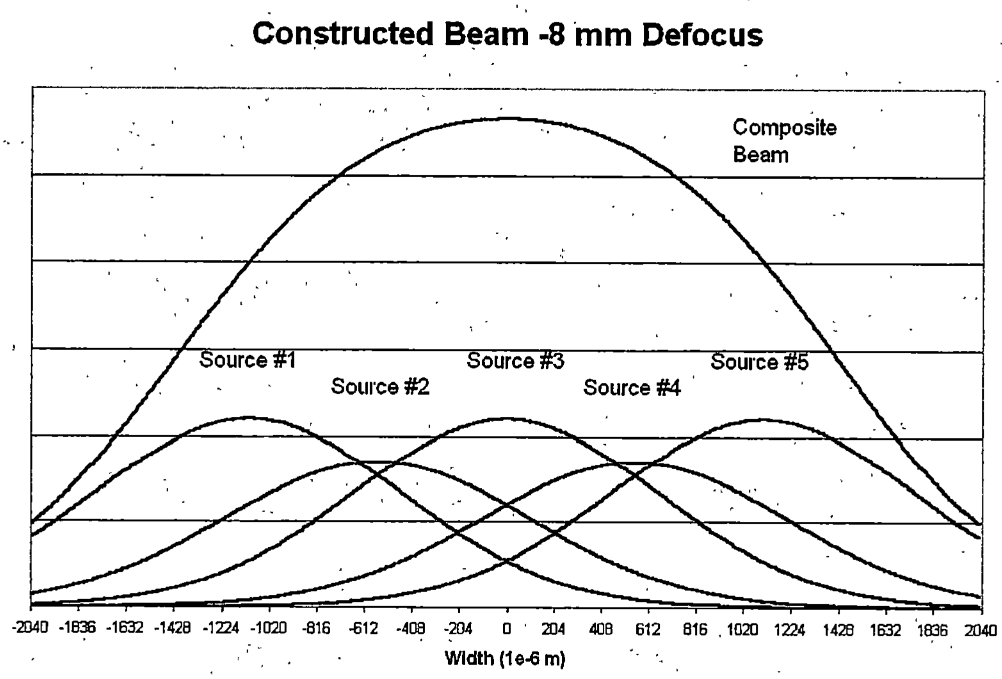

Figure 4.9 Experimental and Constructed Beam Profiles for -8 mm of Defocus

Experimental Beam -9 mm

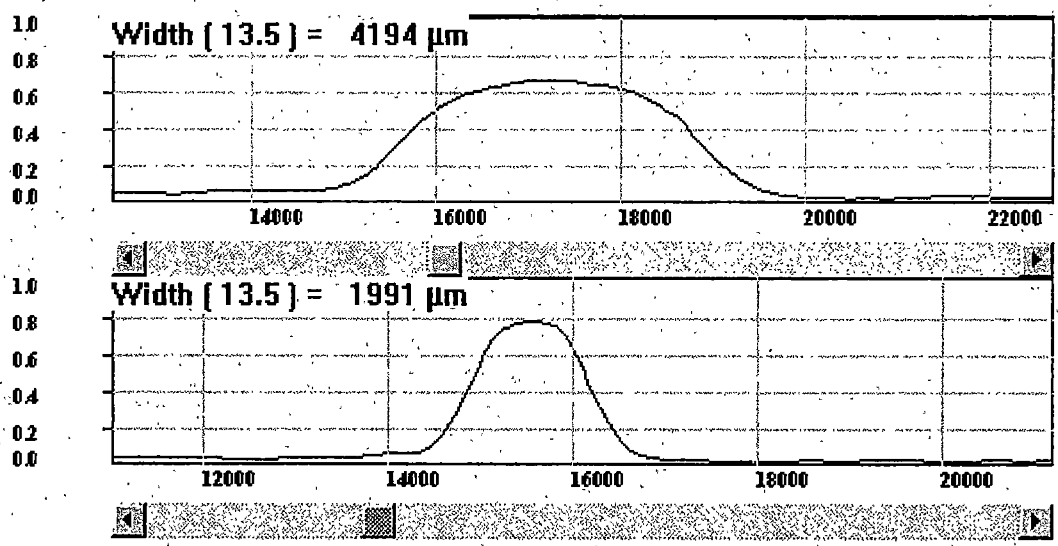

Constructed Beam -9 mm Defocus

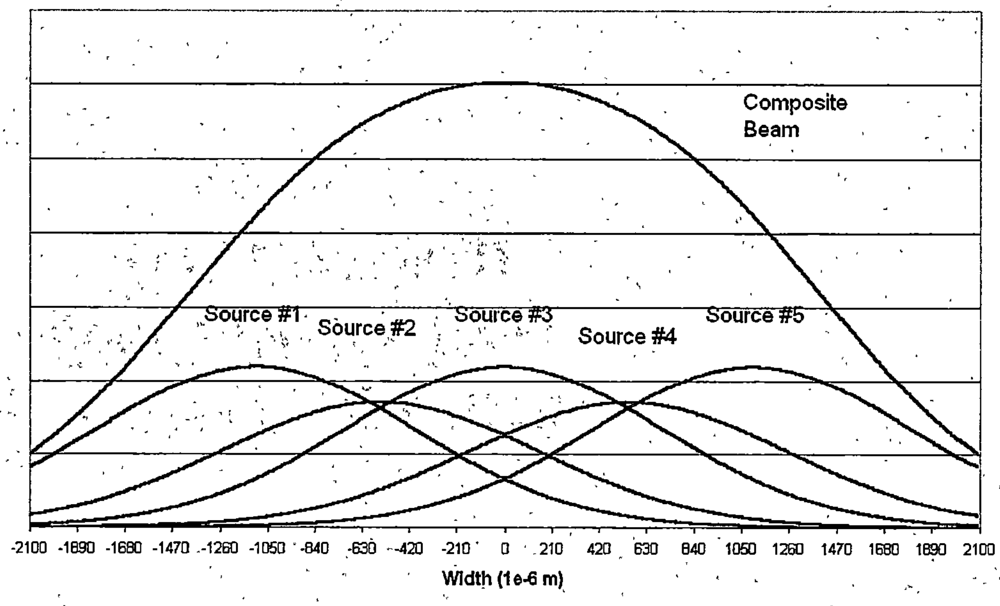

Figure 4.10 Experimental and Constructed Beam Profiles for -9 mm of Defocus

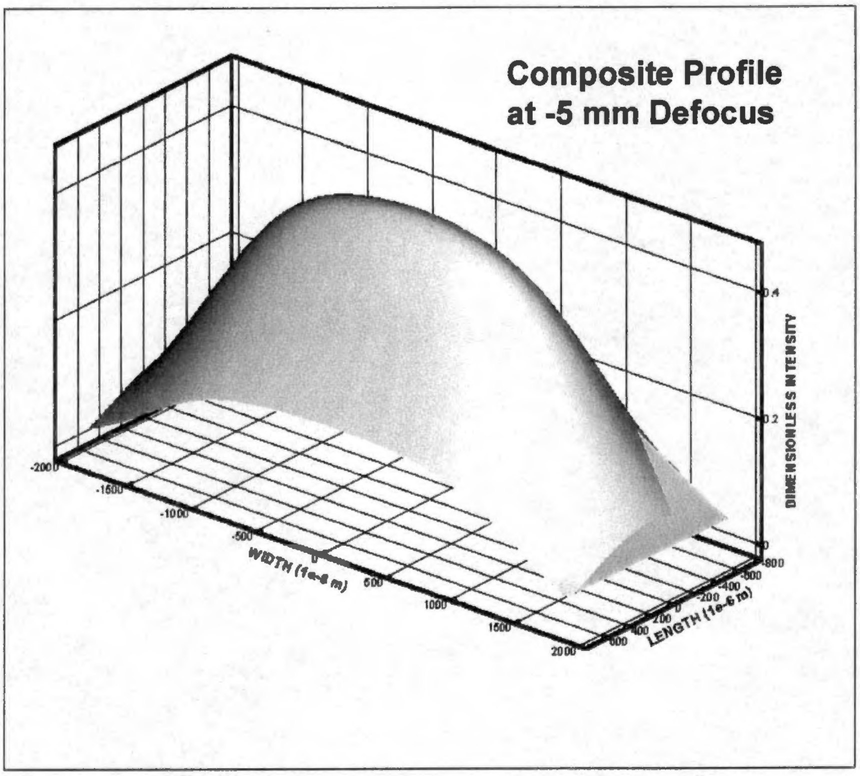

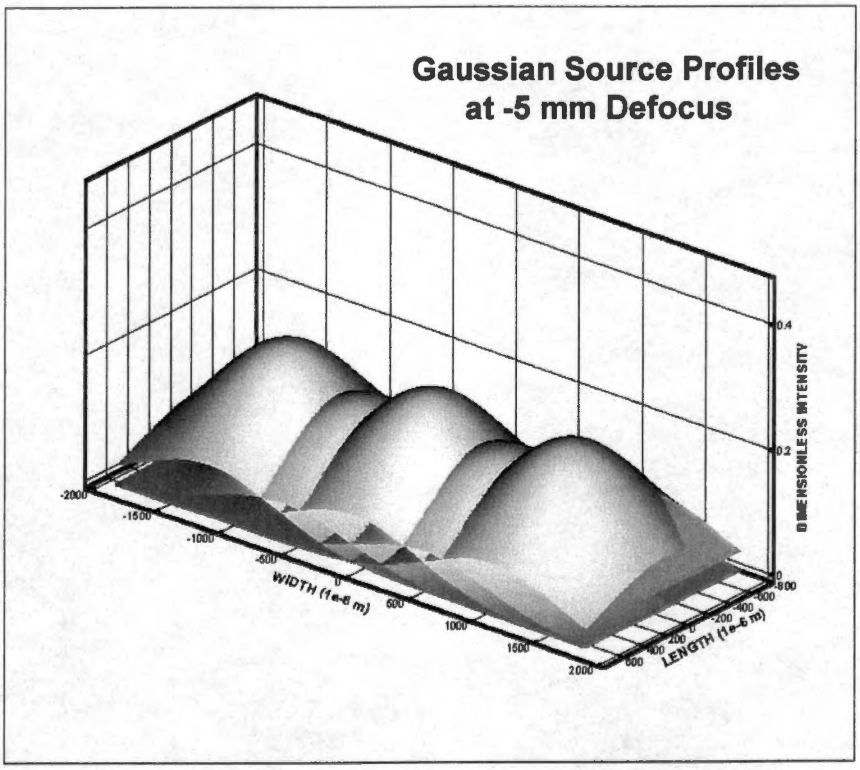

Figure 4.11 Three-Dimensional Plot of Constructed Beam and Gaussian Heat Source Profiles at -5 mm Defocus

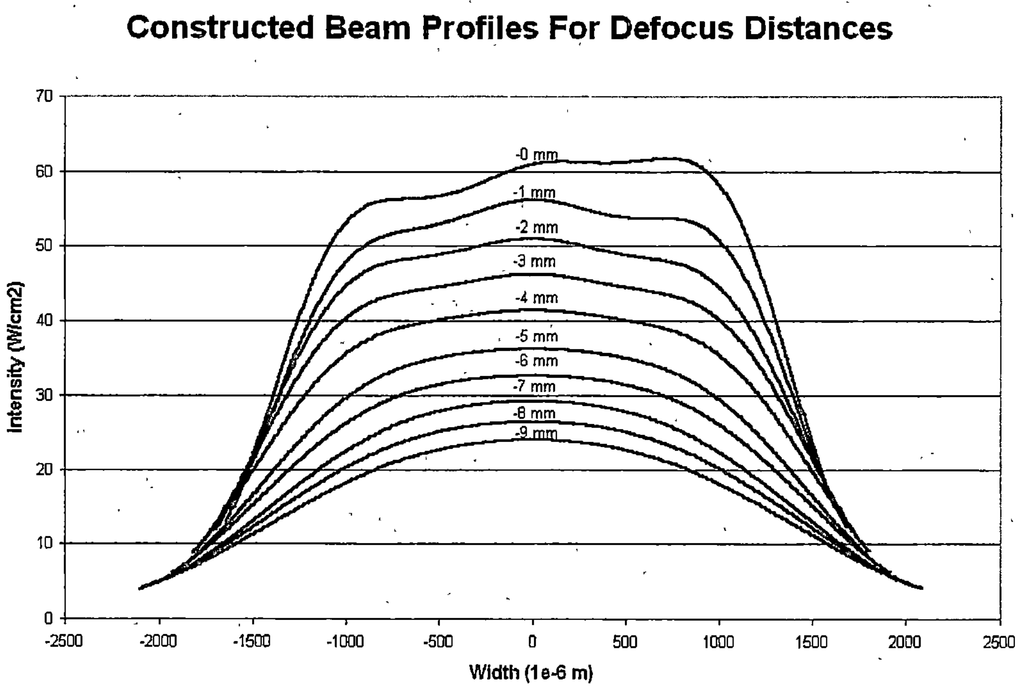

Figure 4.12 Constructed Beam Intensity Profiles at the Width Axis For Defocus Distances

Table 4.1 Radii of Gaussian Heat Sources

Defocus Distance (mm)	Beam Radius r_b (measured to 1/e *peak intensity) (μm)
-0	505
-1	540
-2	575
-3	615
-4	665
-5	740
-6	800
-7	870
-8	930
-9	1000

Table 4.2 Power Percentages, Average Intensity, and Positions for Gaussian Heat Sources

Defocus Distance		Source #1	Source #2	Source #3	Source #4	Source #5
-0	Percentage of 2000 W	21%	16%	21%	19%	23%
	Average Intensity (kW/cm^2)	52.4	39.9	52.4	47.4	57.4
	Position (μm)	-1096	-548	0	548	1096
-1	Percentage of 2000 W	21%	17%	22%	17%	23%
	Average Intensity (kW/cm^2)	45.8	37.1	48.0	37.1	50.2
	Position (μm)	-1102	-551	0	551	1102
-2	Percentage of 2000 W	22%	17%	22%	17%	22%
	Average Intensity (kW/cm^2)	42.4	32.7	42.4	32.7	42.4
	Position (μm)	-1121	-561	0	561	1121
-3	Percentage of 2000 W	22%	17%	22%	17%	22%
	Average Intensity (kW/cm^2)	37.0	28.6	37.0	28.6	37.0
	Position (μm)	-1144	-572	0	572	1144
-4	Percentage of 2000 W	22%	17%	22%	17%	22%
	Average Intensity (kW/cm^2)	31.7	24.5	31.7	24.5	31.7
	Position (μm)	-1150	-575	0	575	1150
-5	Percentage of 2000 W	22%	17%	22%	17%	22%
	Average Intensity (kW/cm^2)	25.6	19.8	25.6	19.8	25.6
	Position (μm)	-1125	-562	0	562	1125
-6	Percentage of 2000 W	22%	17%	22%	17%	22%
	Average Intensity (kW/cm^2)	21.9	16.9	21.9	16.9	21.9
	Position (μm)	-1128	-564	0	564	1128
-7	Percentage of 2000 W	22%	17%	22%	17%	22%
	Average Intensity (kW/cm^2)	18.5	14.3	18.5	14.3	18.5
	Position (μm)	-1096	-548	0	548	1096
-8	Percentage of 2000 W	22%	17%	22%	17%	22%
	Average Intensity (kW/cm^2)	16.2	12.5	16.2	12.5	16.2
	Position (μm)	-1107	-553	0	553	1107
-9	Percentage of 2000 W	22%	17%	22%	17%	22%
	Average Intensity (kW/cm^2)	14.0	10.8	14.0	10.8	14.0
	Position	-1100	-550	0	550	1100

4.3 Calculation of Total Temperature Distribution

In the research performed by Shercliff and Ashby, each Gaussian heat source contributes to the total temperature distribution through superposition with the other Gaussian heat sources used to approximate the experimental laser beam intensity profile. These contributions are found by calculating the temperature distribution from each single Gaussian heat source. From this temperature distribution, a temperature rise can be determined at a point in time and space relative to the coordinates of the single heat source. The temperature rise from the heat sources is summed at each coordinate to simulate the temperature distribution of the material affected by the experimentally measured laser beam. A contribution to the total temperature distribution for an individual Gaussian heat source is calculated by Shercliff and Ashby with the expression,

$$T^* = \frac{(2/\pi)(q^*/v^*)}{[t^*(t^*+1)]^{1/2}} \exp - \left[\frac{(z^*+z_0^*)^2}{t^*} + \frac{y^{*2}}{(t^*+1)} \right] \qquad (4.1)$$

In this equation, y^* represents the distance of the heat source from the beam centerline along its length. The total temperature rise at a point in time and space is calculated by summing these temperature rise contributions and is expressed as,

$$T_t^* = \sum_k^N \frac{(2/\pi)(q_k^*/v^*)}{[t^*(t^*+1)]^{1/2}} \exp - \left[\frac{(z^*+z_0^*)^2}{t^*} + \frac{y_k^{*2}}{(t^*+1)} \right] \qquad (4.2)$$

The y^*_k in the above equation represents a relative distance from a particular source to location of temperature rise. A characteristic length, z^*_0, unique to the experimental laser beam profile is calculated separately as is discussed in the next section. Since a time shift of $t^* = 4x^*/v^*$ is used to assign the position of the Gaussian heat sources along the beam profile length and only one heat source is used to approximate the laser beam profile in that direction, a single value for t^* is used. This value is the time to reach peak temperature, t^*_p, due to the fact that interest lies in the final processing properties and not transient temperature distributions. The time to reach peak temperature is discussed in the next section. A list of the temperature simulation constants that were used is listed in table 4.3 (Shercliff and Ashby 91).

4.4 Characteristic Length Determination Procedure

The characteristic length, z^*_0, is a constant that allows for this temperature distribution simulation to be used for all beam speeds. Its purpose is to essentially limit calculated surface temperature to a finite value equivalent to a peak surface temperature as calculated by a supplementary equation (Shercliff and Ashby 91). As seen in equation (4.1), z^*_0 accomplishes this by offsetting the depth at which the temperature is to be calculated by this characteristic length. This offset creates, in essence, a second surface below the true surface that is used to calculate the temperature distribution. The characteristic length then must be adjusted, or calibrated, in order to model the temperature distribution correctly. The adjustment is conducted through iterative techniques by comparing the calculated peak temperature solution using superposition with a guessed initial z^*_0 to that of a peak temperature solution for the entire experimental

Table 4.3 Temperature Simulation Constants (Shercliff and Ashby 91)

Absorptivity *A*	0.70
Thermal Conductivty λ	25.6 $Js^{-1}m^{-1}K^{-1}$ at 1053 K
Thermal Diffusivity *a*	3.6e-6 m^2s^{-1} at 1053 K
Initial Temperature T_0	300 K
A_1 Temperature A_1	996 K
Melting Temperature T_m	1756 K
Delivered Beam Power *q*	1850 W

laser beam profile using a supplementary expression. The characteristic length is then adjusted until these two peak temperatures agree. A FORTRAN computer program was written to perform this iterative procedure.

An expression which accounts for the complete experimental laser beam profile including its shape, is the peak temperature expression developed by Bass (83) and used by Shercliff and Ashby,

$$T_p^* = (2/\pi^{1/2}) q_R^* / (R v_R^*)^{1/2} \tag{4.3}$$

This equation is valid for cases where v^*_R is much greater than $16R$ and was calculated first by the program. Note this expression is for a uniform intensity rectangular beam. It can be seen that if equation (4.1) is differentiated with respect to t^* and set equal to zero, an expression, for the time to reach peak temperature is found. Since the location of the peak temperature usually occurs at the center of each Gaussian heat source, y^* is set to zero yielding

$$t_p^* = \frac{1}{4}[2(z^* + z_0^*)^2 - 1 + [4(z^* + z_0^*)^4 + 12(z^* + z_0^*)^2 + 1]^{1/2}] \tag{4.4}$$

after differentiation. An initial guessed characteristic length is inserted into the peak time expression (4.4) along with $z^* = 0$ due to the fact that the peak temperature occurs at the surface. This peak time, t^*_p, is then used in place of t^* in equation (4.2). Each temperature contribution from the Gaussian heat sources is found and summed with equation (4.2) to calculate the peak temperature. The position of this peak temperature must be known before its calculation and is determined by using the position of largest laser beam intensity along the width normal to beam velocity. Equations (4.2) and (4.3) are then compared and z^*_0 is adjusted until the values of these equations are within the desired error range. However, equation (4.3) provides a peak temperature based on a uniform rectangular beam profile. This fact reduces the accuracy of the calibration of the characteristic length, which in turn reduces the accuracy of the temperature distribution approximation for highly non-uniform beam profiles.

4.5 Validation of Temperature Simulation Technique

In order to verify the Shercliff and Ashby (91) technique was correctly implemented, several points on figure 1 of the Shercliff and Ashby (91) publication were reproduced. These case depth predications were made using the single Gaussian source temperature distribution technique. This technique uses a peak surface temperature calculation that is different from the one used for the multiple Gaussian source technique as seen with

$$T_p^* = (1/\pi)^{3/2} q^* \tan^{-1}(8/v^*)^{1/2} \qquad (4.5)$$

The reproduced points agreed with Shercliff and Ashby's calculations, and the same technique was used for the calculation of the temperature rises and characteristic length determination for multiple source case.

A one-dimensional heat conduction approximation was used to roughly predict the extent of heat conduction into the material. The heat conduction approximation is given by

$$\frac{T - T_s}{T_0 - T_s} = erf\left(\frac{z}{2\sqrt{at}}\right) \qquad (4.6)$$

where T is the temperature rise, T_s is the surface temperature, T_0 is the initial temperature, z is the depth, a is the thermal diffusivity, and t is the time the surface temperature acts on the surface (Wong 77). The surface temperature was calculated using equation 4.3, and the interaction time, $2r_b/v$, was used for the time of conduction. A plot of the temperature rise depths for defocus distances of –0 mm and –9 mm is shown in figure 4.13. Interaction times used were 1.21 s for the –0 mm defocus case and 2.40 s for the –9 mm case. During these interaction times, the maximum depth of a temperature rise is about 4.00e-4 m or 0.04 cm. The thickness of the workpiece used was 0.635 cm, and the ratio of the maximum heat conduction depth to the workpiece thickness is 0.063 or 6.3%. This shows that a semi-infinite domain temperature distribution model would be valid for the workpiece geometry because 0.04 cm << 0.635 cm.

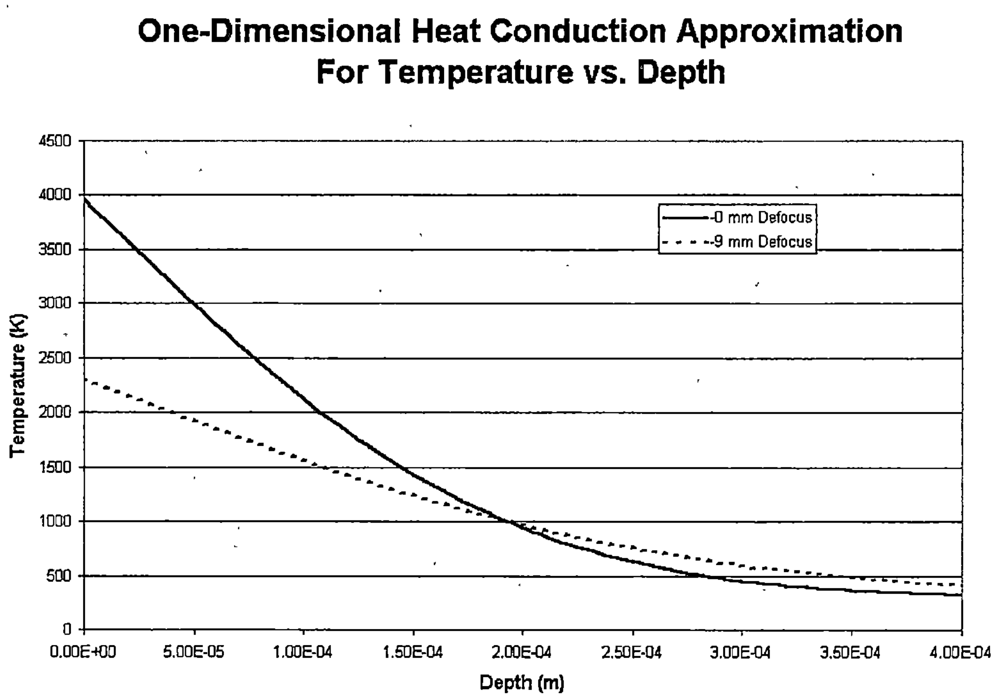

Figure 4.13 One-Dimensional Heat Conduction Approximation of Temperature vs. Depth

Chapter 5

Results

This chapter includes the data resulting from the experiments and temperature distribution simulations conducted during this research. Included in the experimental data are layer and HAZ depth measurements along with processed sample cross-section images. The experimental data are analyzed and related to needed vertical transverse times and velocities. The data include temperature distribution melt profile plots. A comparison of temperature distribution and experimental results and an investigation of the temperature simulation technique are also presented.

5.1 Description of Experimental Results

The range of processing trials for the experimental section of this research corresponds to the optimum focus distance of 115 mm from the focusing optics through 1 mm increments to a focus distance of 9 mm shorter than optimum focus distance totaling ten trials. It should be noted that the optimum focus distance was determined from previous laboratory research experience and is not equivalent to the true focus distance of the focusing optics. Three tracks were processed for each trial under the same conditions. The materials used, operating conditions, and metallurgical analysis are as described in Chapter 4. Using a microscope, the image of the cross-section for each trial was taken and presented. Alloyed layer and HAZ measurements were taken from the mid-point of all processed track widths and vertically from the alloyed layer top surface.

5.2 Processed Track Cross-Sectional Images

After each trial was cross-sectioned, mounted, ground, polished, and etched as described in Chapter 5, digital images of the processed tracks were created. Each image was made at various magnification values. Although three tracks were processed and analyzed for each trial, one image for each trial is presented due to the fact that all three tracks for each trial were very similar in appearance and proportion. In each image the processed layer zone and the HAZ has been indicated, however, variations in the etching process resulted in the HAZ seemingly consisting of multiple zones for some trials. In these trials the HAZ extends down to the lowest point where the HAZ microstructure appears different from the base material's microstructure. An area of pronounced increased layer depth located to one side of the processed layers can be noted. The cause of this asymmetry is generally unknown but could be contributed to convective circulation eddies in the molten layer zone during processing (Drazin and Reid 81). This idea is supported by the fact that the lower boundary does not display this pronounced area of increased depth, and the area decreases with a decreased molten layer depth as seen in the trials with shorter focus distances. A slight misalignment of the focusing optics, which caused an area of higher intensity to one side of the beam profile, was noted in the beam profile analysis. This area might intensify eddy circulation to one side of the processed track. The images for the experimental processing trials are presented in figures 5.1-5.5.

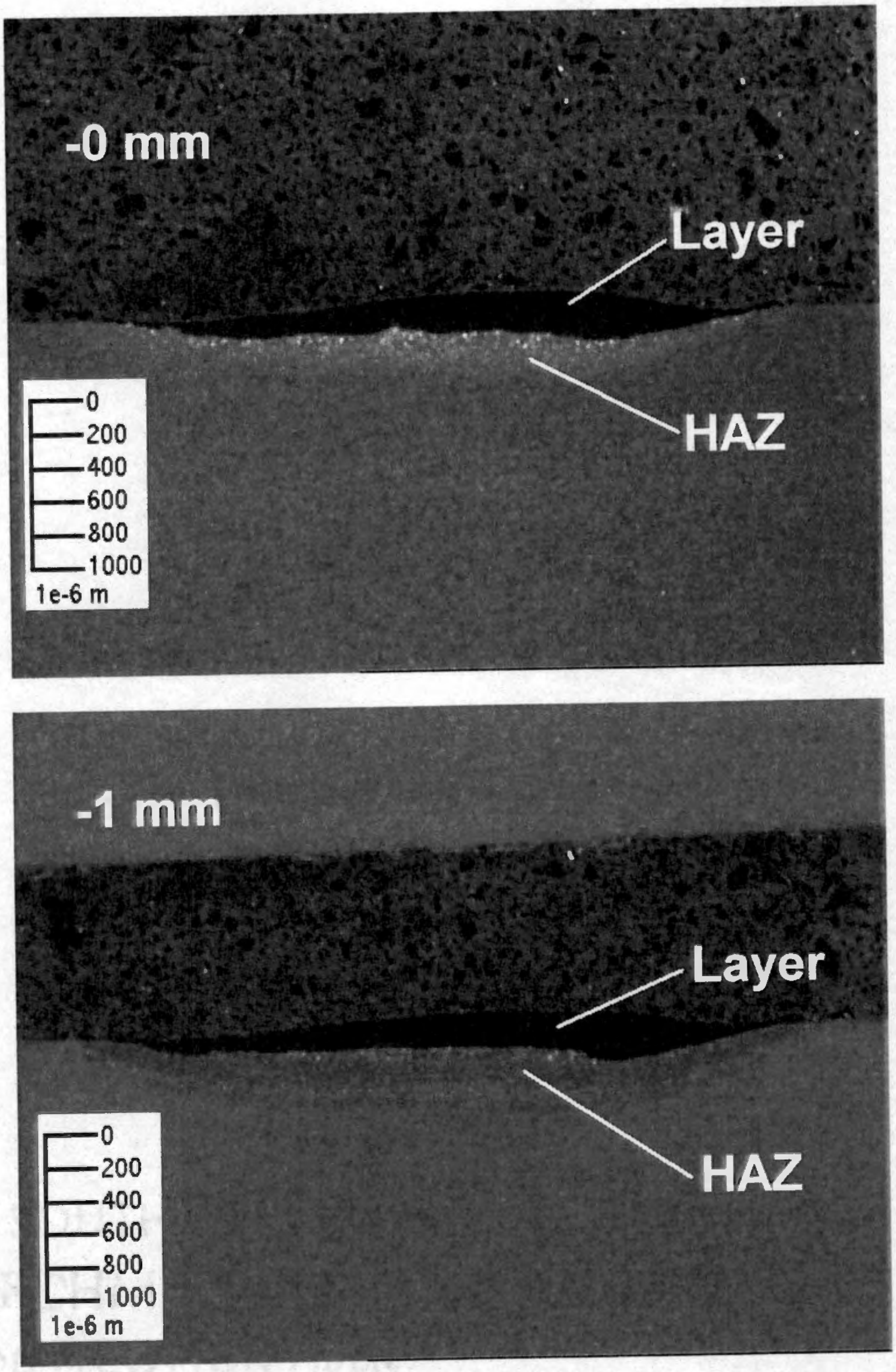

Figure 5.1 Experimental Trial Cross-Section for -0 mm and -1 mm Defocus

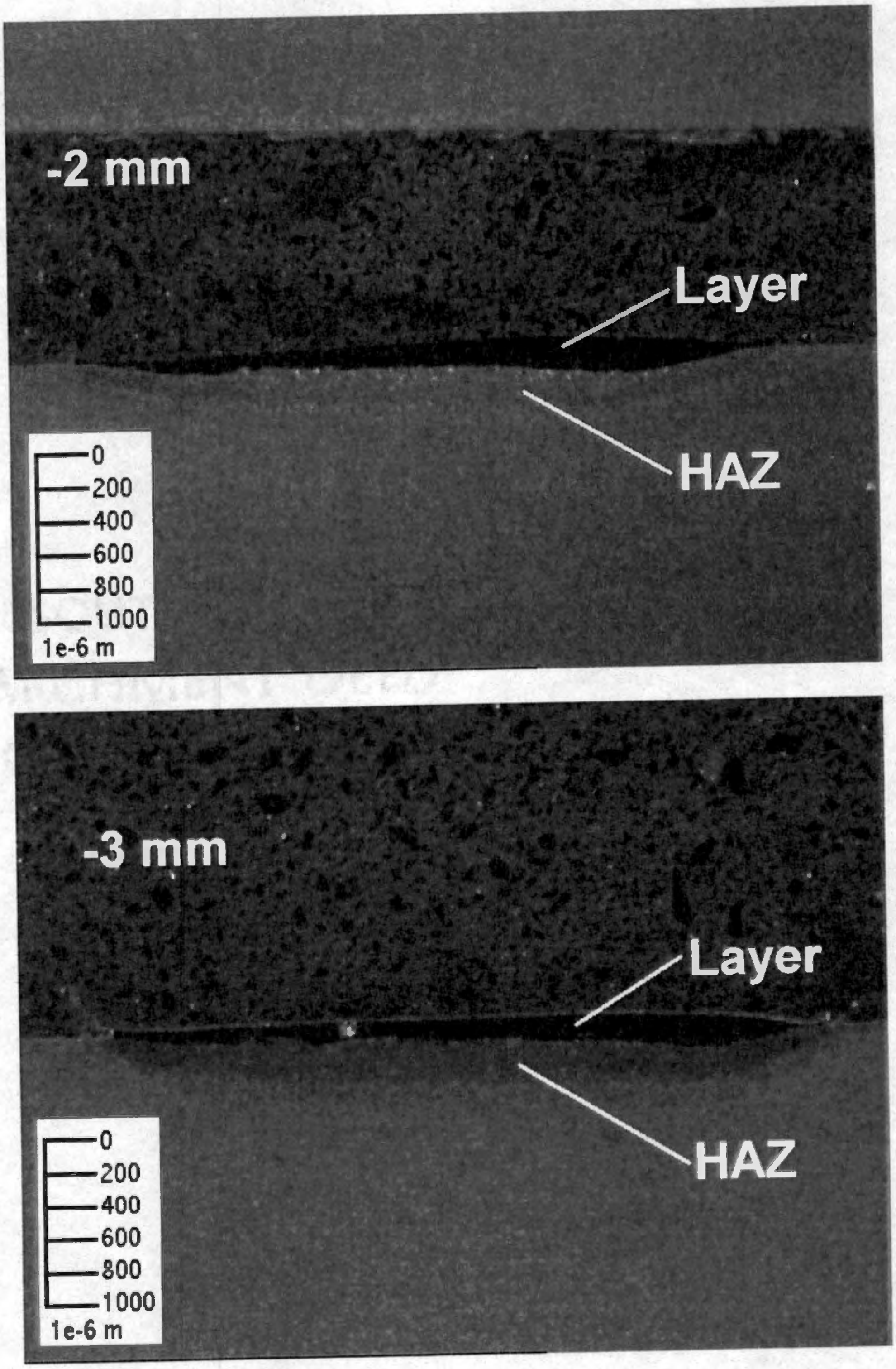

Figure 5.2 Experimental Trial Cross-Section for -2 mm and -3 mm Defocus

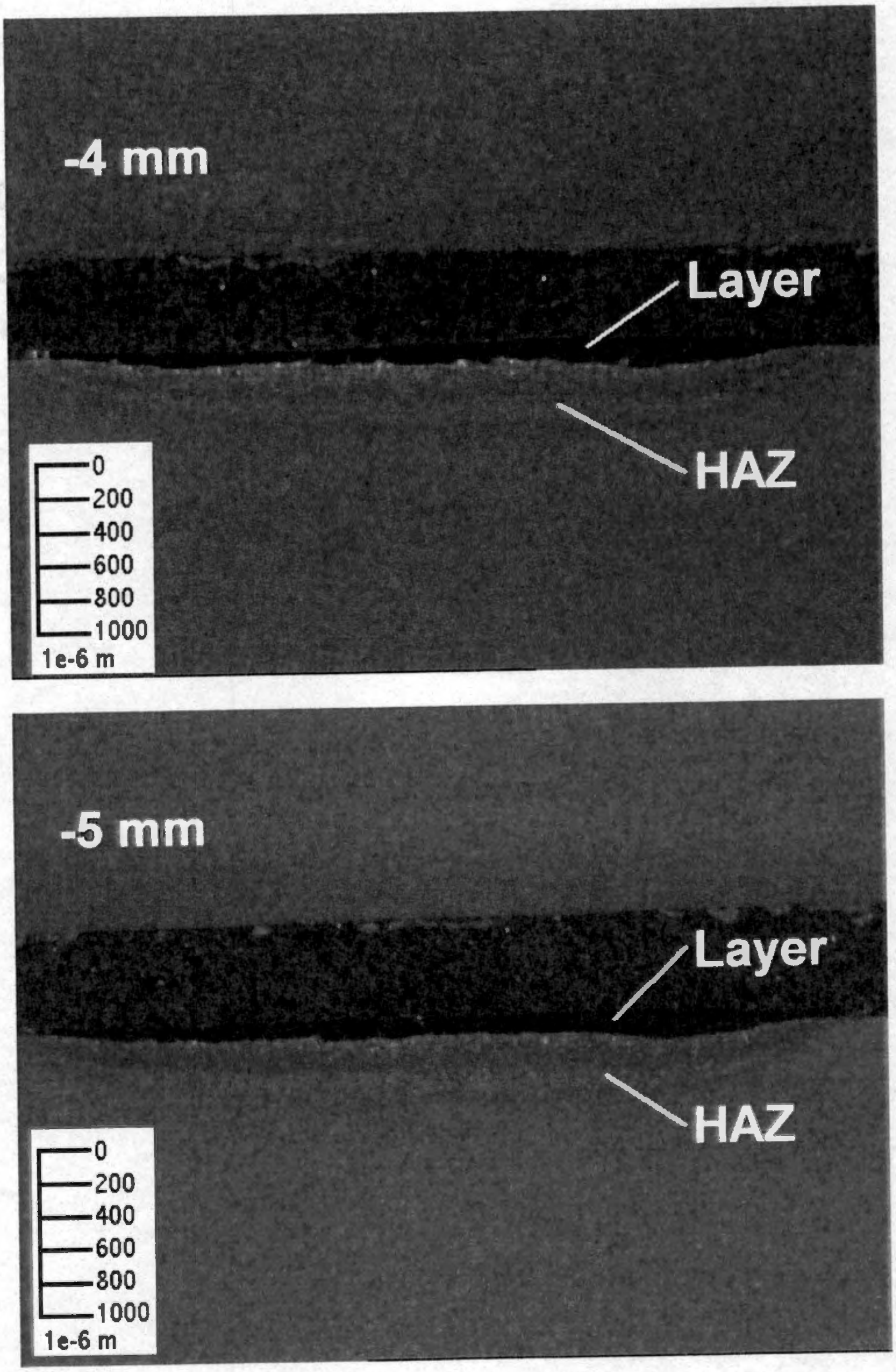

Figure 5.3 Experimental Trial Cross-Section for -4 mm and -5 mm Defocus

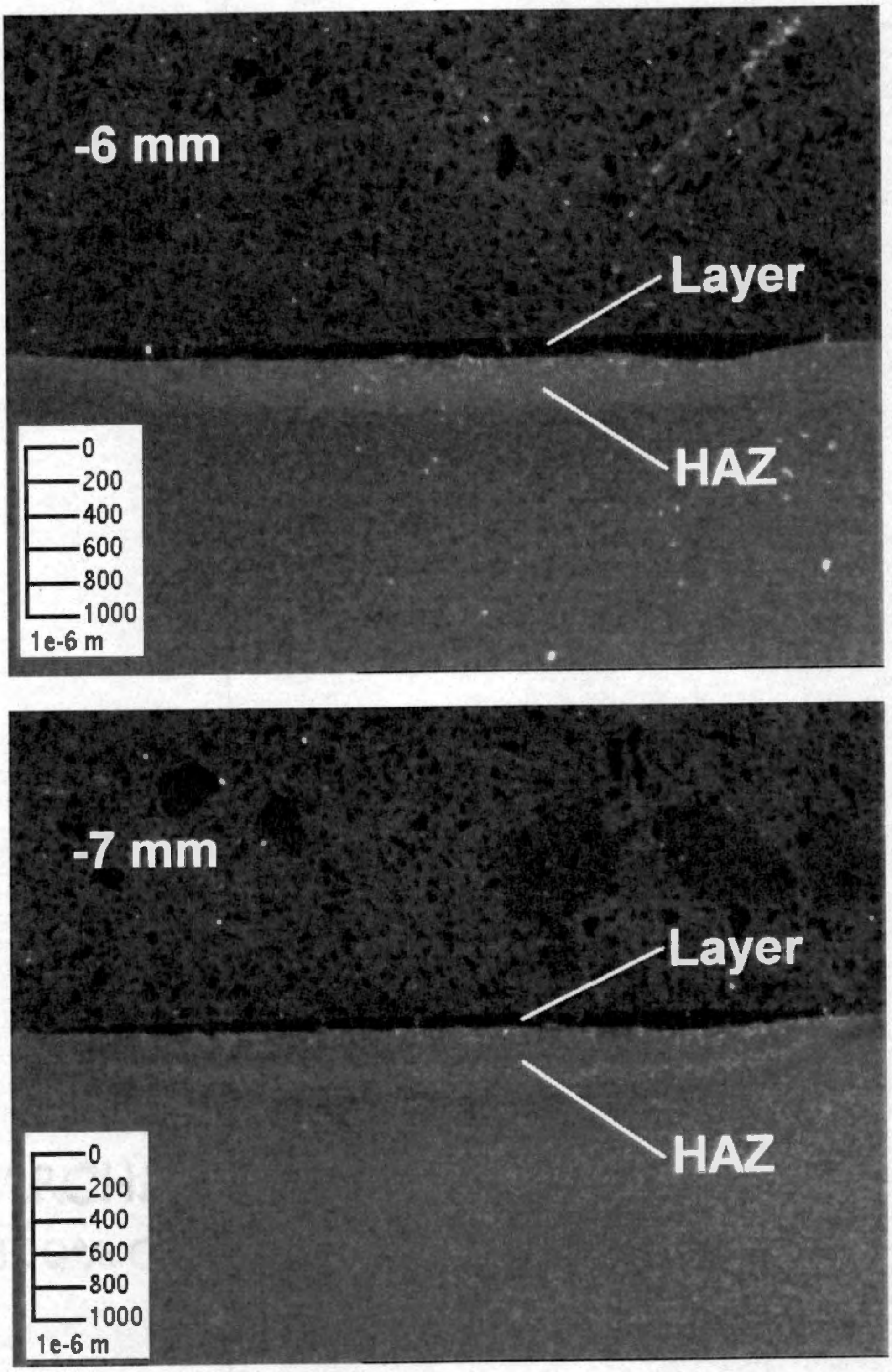

Figure 5.4 Experimental Trial Cross-Section for -6 mm and -7 mm Defocus

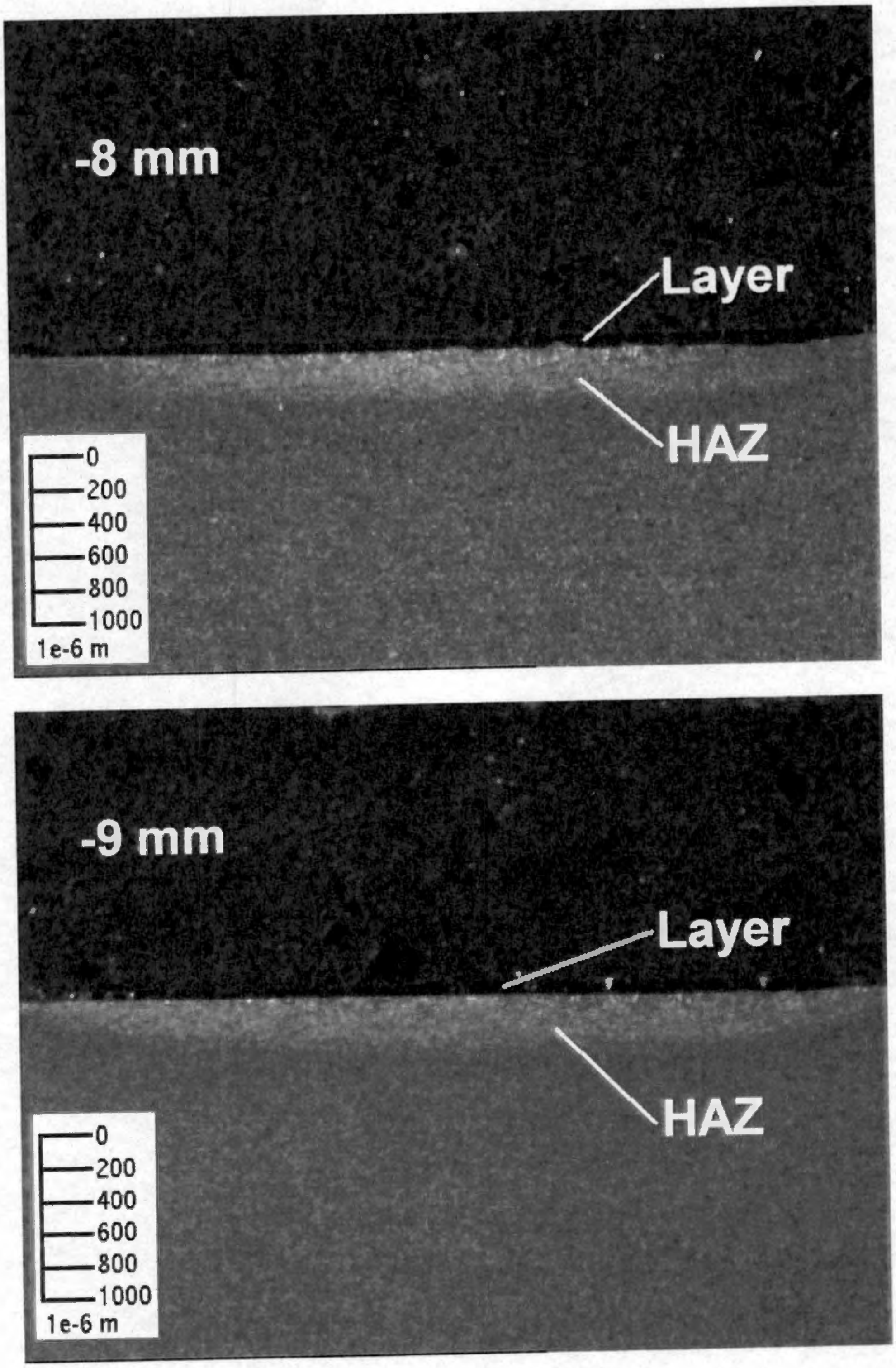

Figure 5.5 Experimental Trial Cross-Section for -8 mm and -9 mm Defocus

5.3 Melt Zone Depth and HAZ Depth Measurements

As detailed in Chapter 4, each depth of the melt zone and the HAZ was measured from the alloyed layer surface and in the center of the track. These measurements were made with a microscope and the appropriate scale. The depths of the melt zone and the HAZ for each of the three tracks of a trial were averaged to give the overall melt zone depth and HAZ depth measurement for the trial. The measurements are presented in numerical form in table 5.1 and in graphical form in figure 5.6 that also contains the melt and HAZ depth measurements as a function of beam intensity.

5.4 Experimental Data Analysis

By examining the images of the cross-sections of the experimental trials, the quality of the final processing characteristics can be determined. These characteristics can be further supported by the layer and HAZ depth measurements. One example of a final processing characteristic is the processed layer's geometry. The processed layer's geometry at optimum processing focus is considered ideal, so all other trials were compared to the ideal for similarity in geometry. An example of a desired final processing characteristic is the proper mix of precursor components into the melted base metal. The ratio of this mixture can be expressed by comparing the thickness of the processed layer at optimum focus distance with all other trials since the precursor thickness and, thus, the unit volume, is relatively equal for all trials. This comparison is shown in table 5.2. As an example, the limit for defocusing appears to be -4 mm of defocus since the melt depth of 100 μm and the HAZ depth μm of 352 compare well with

Table 5.1 Layer and HAZ Depth Measurements From Track Midpoint

Defocus Distance mm		Track #1 Depth µm	Track #2 Depth µm	Track #3 Depth µm	Average Depth µm	Standard Deviation µm	Average Layer Depth/ Average HAZ Depth
-0	Layer	180	180	180	180	0	0.400
	HAZ	450	450	450	450	0	
-1	Layer	155	155	155	155	0	0.363
	HAZ	425	430	425	427	3	
-2	Layer	140	140	140	140	0	0.352
	HAZ	400	400	395	398	3	
-3	Layer	125	120	120	122	3	0.325
	HAZ	375	375	375	375	0	
-4	Layer	100	100	100	100	0	0.284
	HAZ	355	350	350	352	3	
-5	Layer	85	85	85	85	0	0.256
	HAZ	330	335	330	332	3	
-6	Layer	75	75	75	75	0	0.248
	HAZ	300	310	300	303	6	
-7	Layer	65	60	65	63	3	0.229
	HAZ	275	275	275	275	0	
-8	Layer	50	55	50	52	3	0.212
	HAZ	245	245	245	245	0	
-9	Layer	45	45	50	47	3	0.207
	HAZ	230	225	225	227	3	

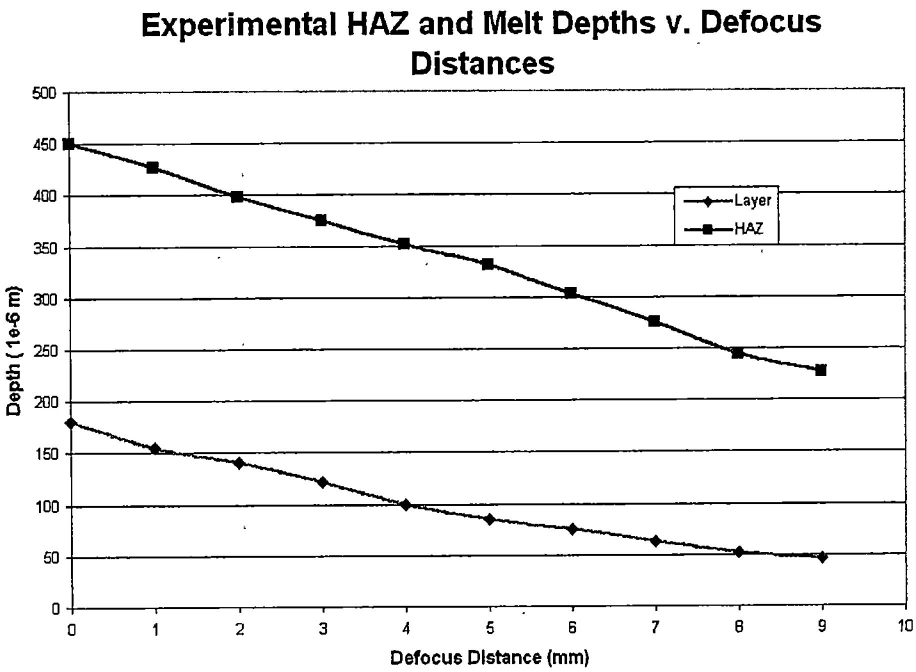

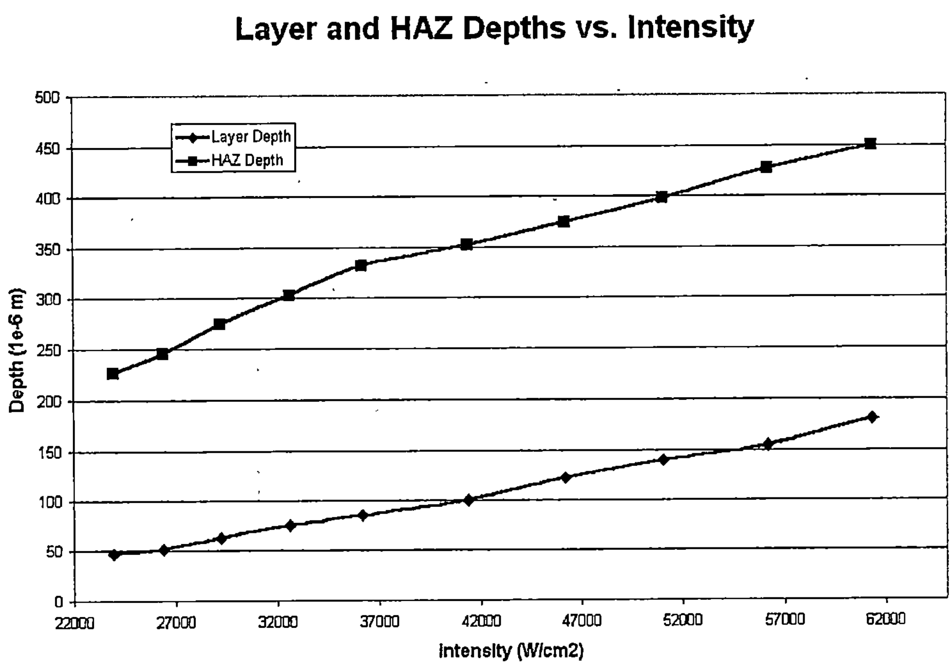

Figure 5.6 Measured Layer and HAZ Depths vs. Defocus Distances and Beam Intensity at 2000 W, 5000 mm/min

Table 5.2 Comparison of Layer and HAZ Depths

Defocus Distance mm	Layer Depth Percentage	HAZ Depth Percentage	Layer/HAZ Depth Ratio Percentage
-0	100%	100%	100%
-1	86.11%	94.89%	90.75%
-2	77.78%	88.44%	87.95%
-3	67.78%	83.33%	81.34%
-4	55.56%	78.22%	71.03%
-5	47.22%	73.78%	64.00%
-6	41.67%	67.33%	61.89%
-7	35.00%	61.11%	57.27%
-8	28.89%	54.44%	53.07%
-9	26.11%	50.44%	51.76%

the ideal. The layer and HAZ depth percentages of 56% and 78% of those at optimum processing focus, respectively, are acceptable for providing a sufficient mix of precursor components with the base metal. These requirements are somewhat application dependent, and thus, this limit of defocusing is a general example.

As noted in figure 5.6, the plots of melt and HAZ depth as functions of defocus distance and intensity reveal a linear relationship between the melt and HAZ depths and intensity and defocus distance. The melt and HAZ depths decrease with and increase in defocus distance by a slope of –13.3 μm/mm and –22.3 μm/mm respectively. Increases in melt and HAZ depths with an increase in intensity are shown in the plots with change of about 3.57 μm/kW/cm^2 for the melt depth and about 5.97 μm/kW/cm^2 for the HAZ depth.

5.5 Focus Correction Analysis

Given the processing velocity, the time allowed to correct a focus distance from defocus to optimum focus can be found if the required horizontal resolution is known. The horizontal resolution is defined as the length parallel to the processing direction that the beam moves as a focus distance correction is performed. This length can be used to determine the minimum horizontal size of a surface fluctuation that can be successfully corrected. A limit for the correction time can be found by dividing the horizontal resolution by the processing velocity. Correction time plots for various processing velocities and horizontal resolutions are shown in figure 5.7. The response time of the distance measuring device and computer system would have to be added to this correction time to represent an accurate value of the time needed to make a correction.

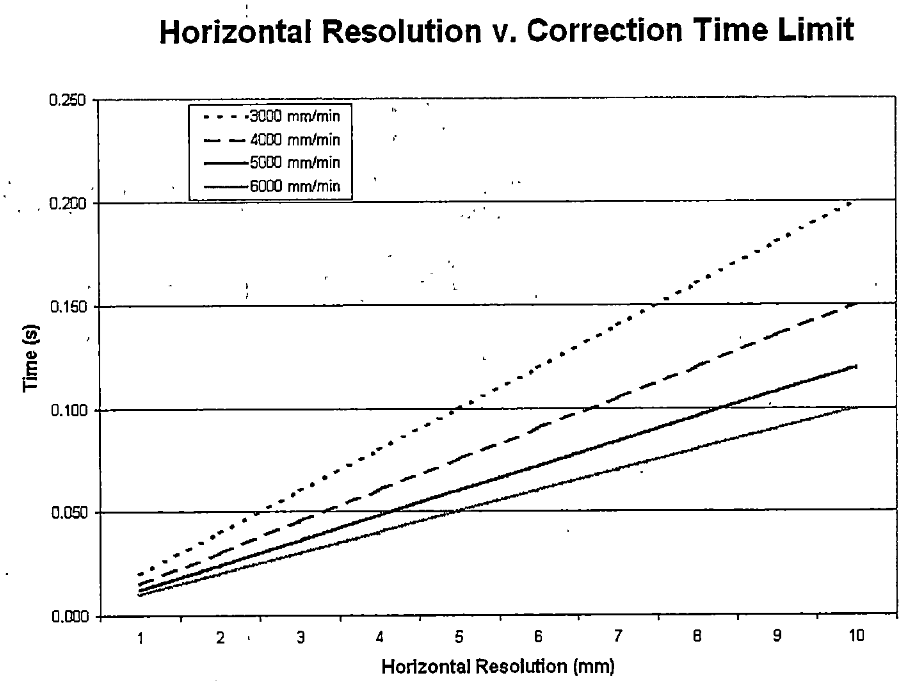

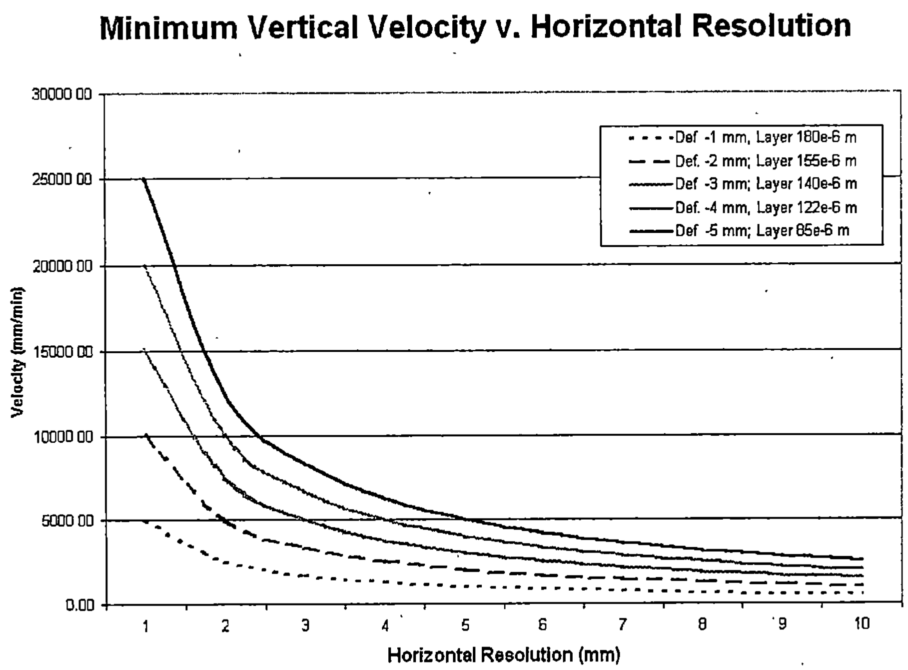

Figure 5.7 Graphs of Correction Times and Minimum Vertical Velocities

An example of these response times are around 0.512 ms for an optical based distance measuring device (Keyence website) and around 1 ms for the controller card (Aerotech catalog) which totals approximately 0.0015 s. Using the horizontal resolution as the sole determination of the correction time limit, a minimum vertical velocity needed to correct a certain defocus distance can be determined by dividing the defocus distance by the correction time. This minimum vertical velocity assumes constant velocity and does not account for acceleration. The required vertical velocities for various defocus distances at a processing velocity of 5000 mm/min are plotted in figure 5.7. If the maximum amount of defocus is -4 mm as determined above and the needed horizontal resolution is 5 mm, the correction time limit would be around 0.06 s. The corresponding required vertical velocity would be 66.66 mm/s or 4000 mm/min. The vertical stage would at the very least need to translate at 4000 mm/min. However, in realistic terms this vertical velocity would need to be around 100 mm/min greater to compensate for the response time lag of approximately 0.0015 s in the systems mentioned above.

If a surface contour changes along the processing path, these changes can be expressed as the distance change in the vertical direction z related to the distance change in the processing direction x or dz/dx as shown in figure 5.8. The rate of the change in the x direction is the processing velocity or dx/dt. This rate of change can be related to the rate of the change in the vertical direction by

$$\frac{dz}{dt} = v\frac{dx}{dy} \tag{5.1}$$

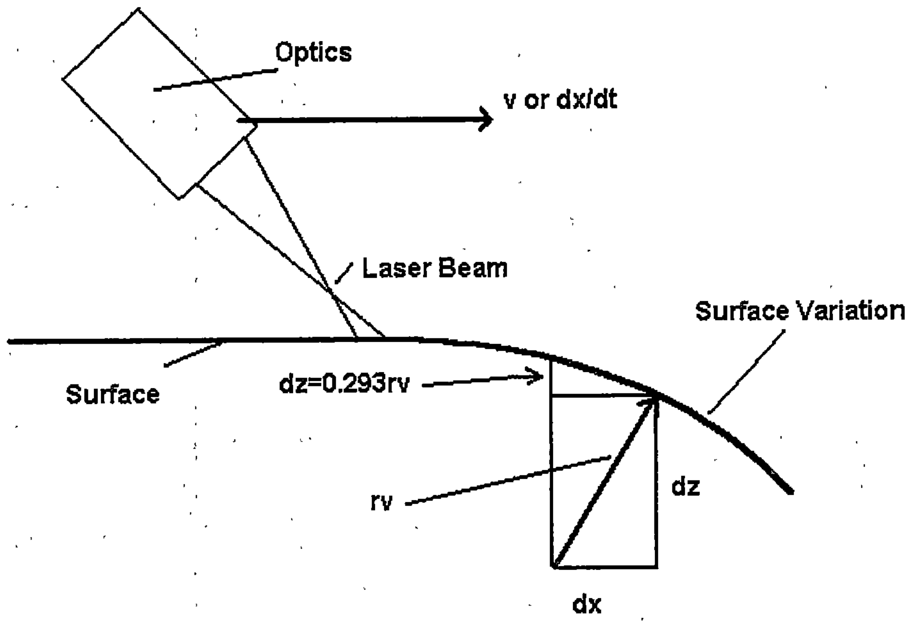

Figure 5.8 Schematic of Focus Correction Parameters

Each surface contour variation can said to have a radius of curvature, which is noted by r_v. The radius of curvature is shown at a 45° degree angle from horizontal in figure 5.8. At this angle, the dx and dz equal 0.707 times r_v. When the angle of r_v is 90°, dz is at its maximum and is equal to r_v. The change in the vertical distance over the angles between 45°-90° is

$$dz = r_v - 0.707 r_v = 0.293 r_v \qquad (5.2)$$

So, if dz/dt can match dx/dt, variations of radius 1/0.293 or 3.50 times dx or the horizontal resolution can be corrected. If, for example, a variation of radius 10 mm were encountered, the horizontal resolution would need to be 2.85 mm. At a processing velocity of 5000 mm/min, a vertical velocity of 292 mm/s or 17454 mm/min would be required for this example.

The current motion system maximum vertical and horizontal velocity is 305 mm/s or 18300 mm/min (Techno-Isel catalog). The current hardware capacity is more than adequate to correct a defocus distance of -4 mm with a horizontal resolution of 5 mm and is sufficient to correct a defocus distance of -10 mm with a horizontal resolution of 2.85 mm.

5.6 Temperature Distribution Simulation Results

Using the temperature distribution simulation technique developed by Shercliff and Ashby (91), temperature distributions were simulated for the ten focus distances. These distances include the optimum processing focus distance of 115 mm as determined from previous experience through a distance of 9 mm shorter than optimum processing focus distance in 1 mm increments (Schwartz 00). In each trial, the normalization constant, which is the same as the beam radius r_b, for the spatial coordinates is unique. By limiting the levels of temperatures represented in the temperature distribution simulations to that of the eutectoid (transformation) and melt temperatures, the simulated HAZ and melt profiles are plotted. All simulations consist of 500 data points along the width dimension and 100 data points along the depth dimension. Each simulation represents the temperature distribution at the dimensionless time to reach peak temperature for that laser beam profile as discussed in Chapter 4.

5.7 Melt and HAZ Temperature Simulation Profiles

Using a melt temperature of 1756 K and a eutectoid temperature of 996 K, melt and HAZ profiles were plotted from the temperature simulation results in figures 5.9-5.13. In the plots, the melting and eutectoid temperatures are dimensionless values of 1.00 and 0.48 respectively. Simulated temperatures corresponding to these values were used as boundaries between the melt zone, HAZ and the unaffected base metal. The dimensions used in the simulation plots are dimensionless as well with the normalization constants shown.

5.8 Comparison of Results

Simulated melt and HAZ depths with dimensions of μm were determined by examining the temperature distribution simulation results and noting the depth at which the melting and HAZ temperatures occur at the center of the track. These dimensionless

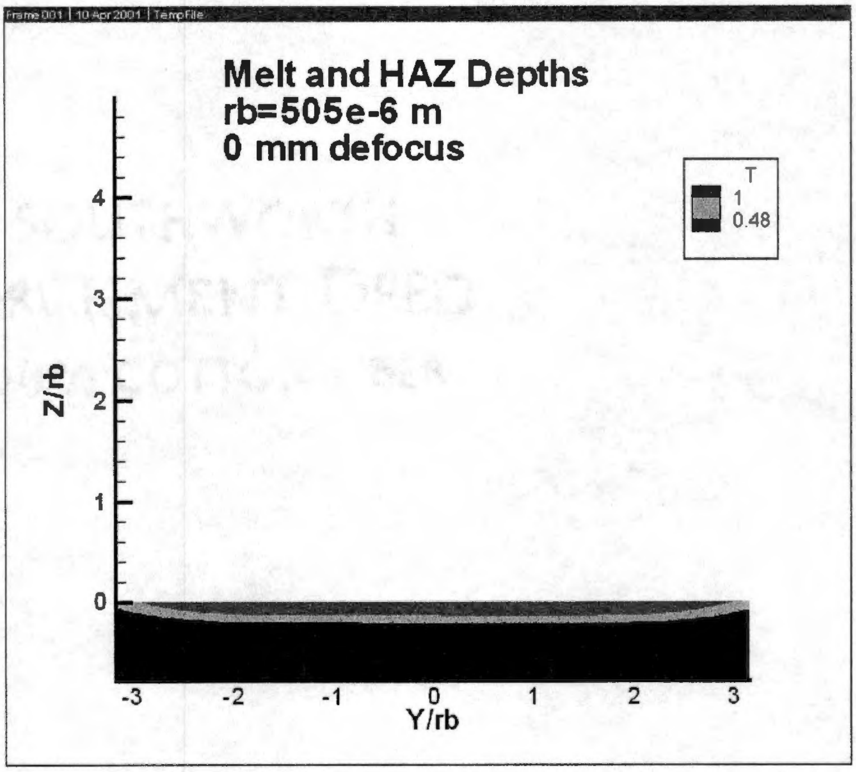

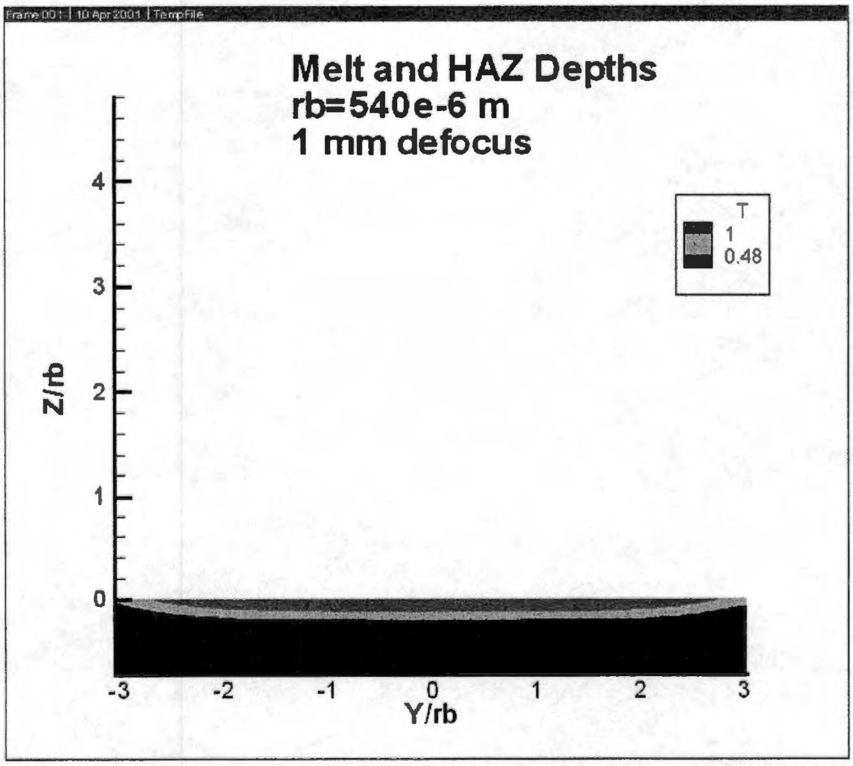

Figure 5.9 Melt and HAZ Profiles for -0 mm and -1 mm Defocus Distance at 2000 W, 5000 mm/min

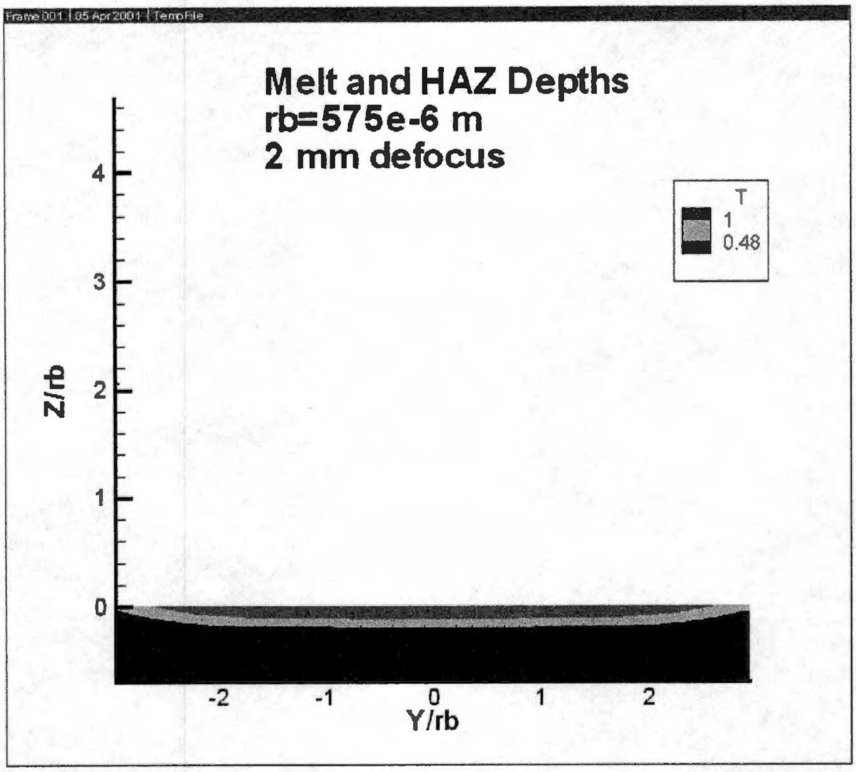

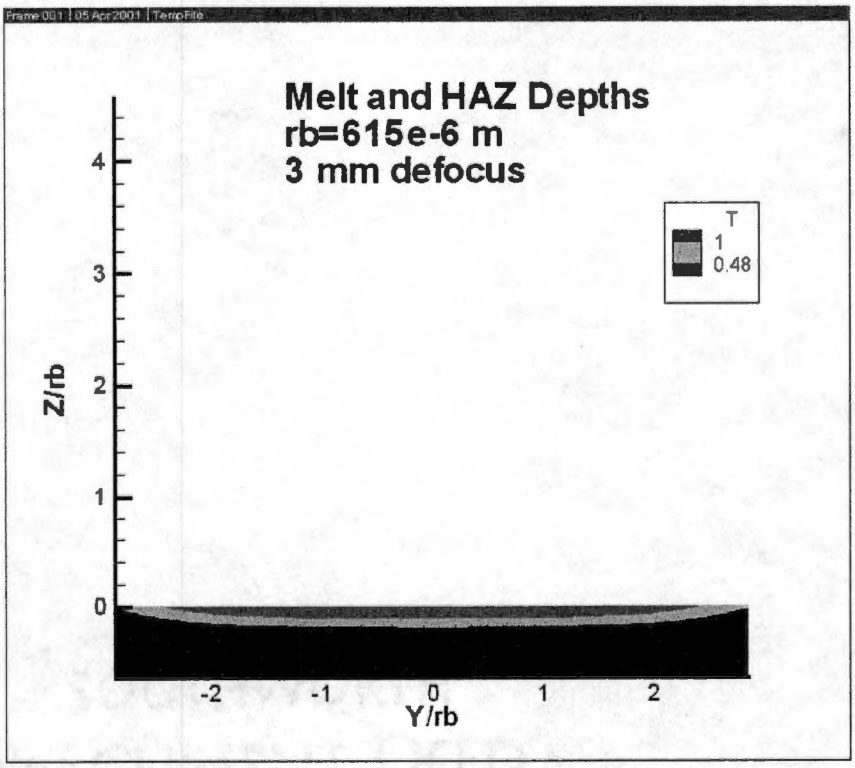

Figure 5.10 Melt and HAZ Profiles for -2 mm and -3 mm Defocus Distance at 2000 W, 5000 mm/min

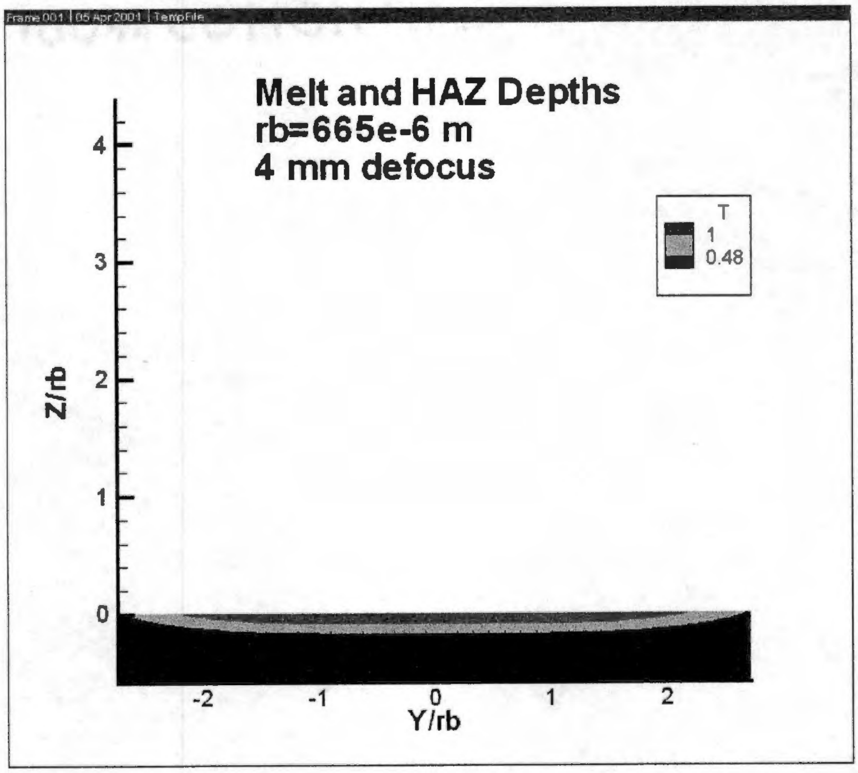

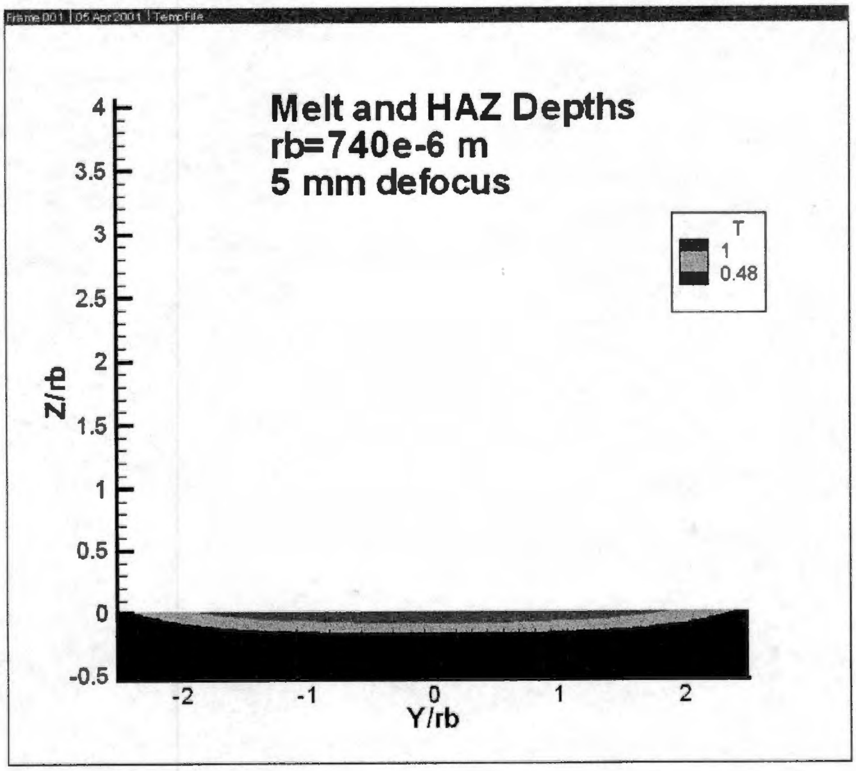

Figure 5.11 Melt and HAZ Profiles for -4 mm and -5 mm Defocus Distance
at 2000 W, 5000 mm/min

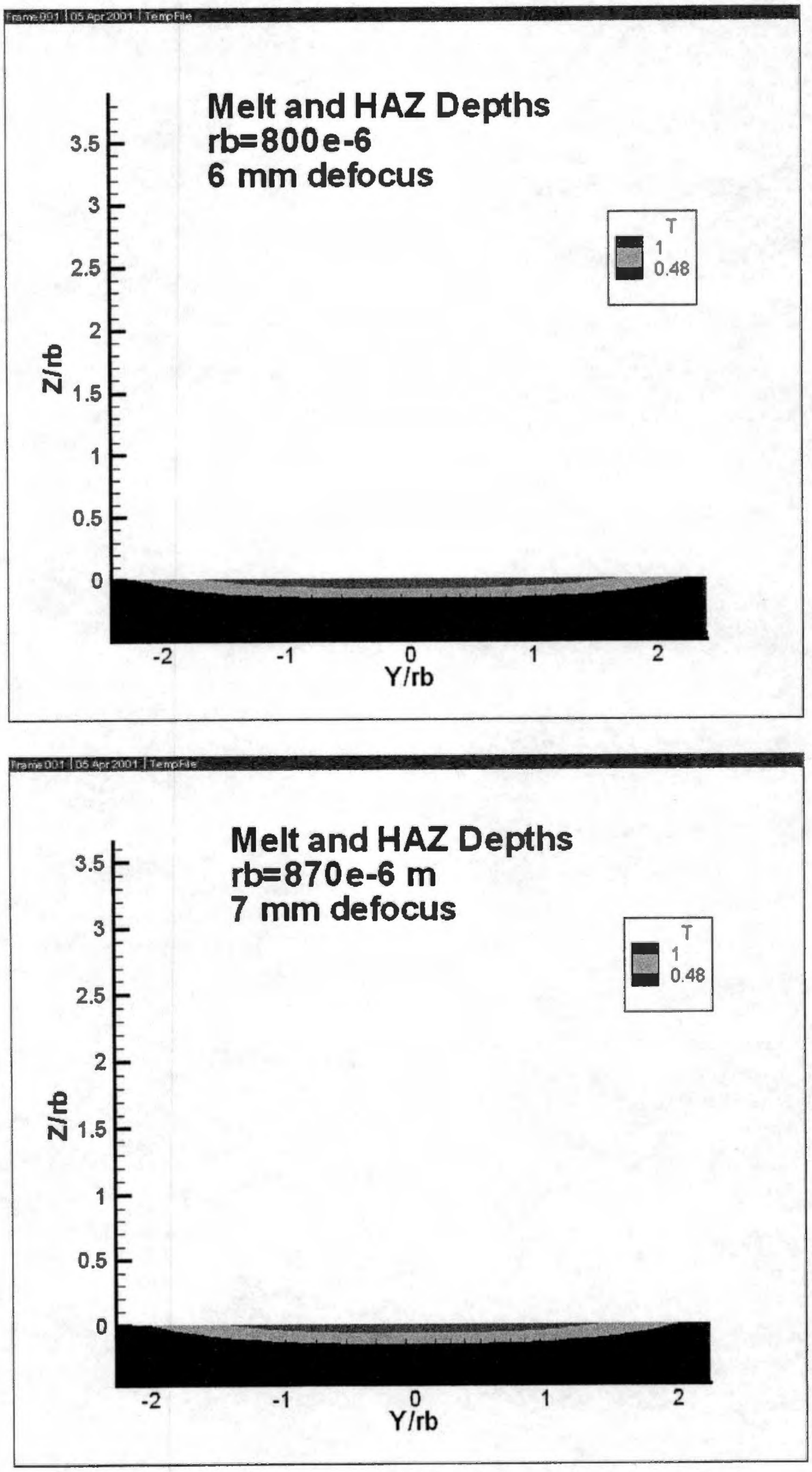

Figure 5.12 Melt and HAZ Profiles for -6 mm and -7 mm Defocus Distance at 2000 W, 5000 mm/min

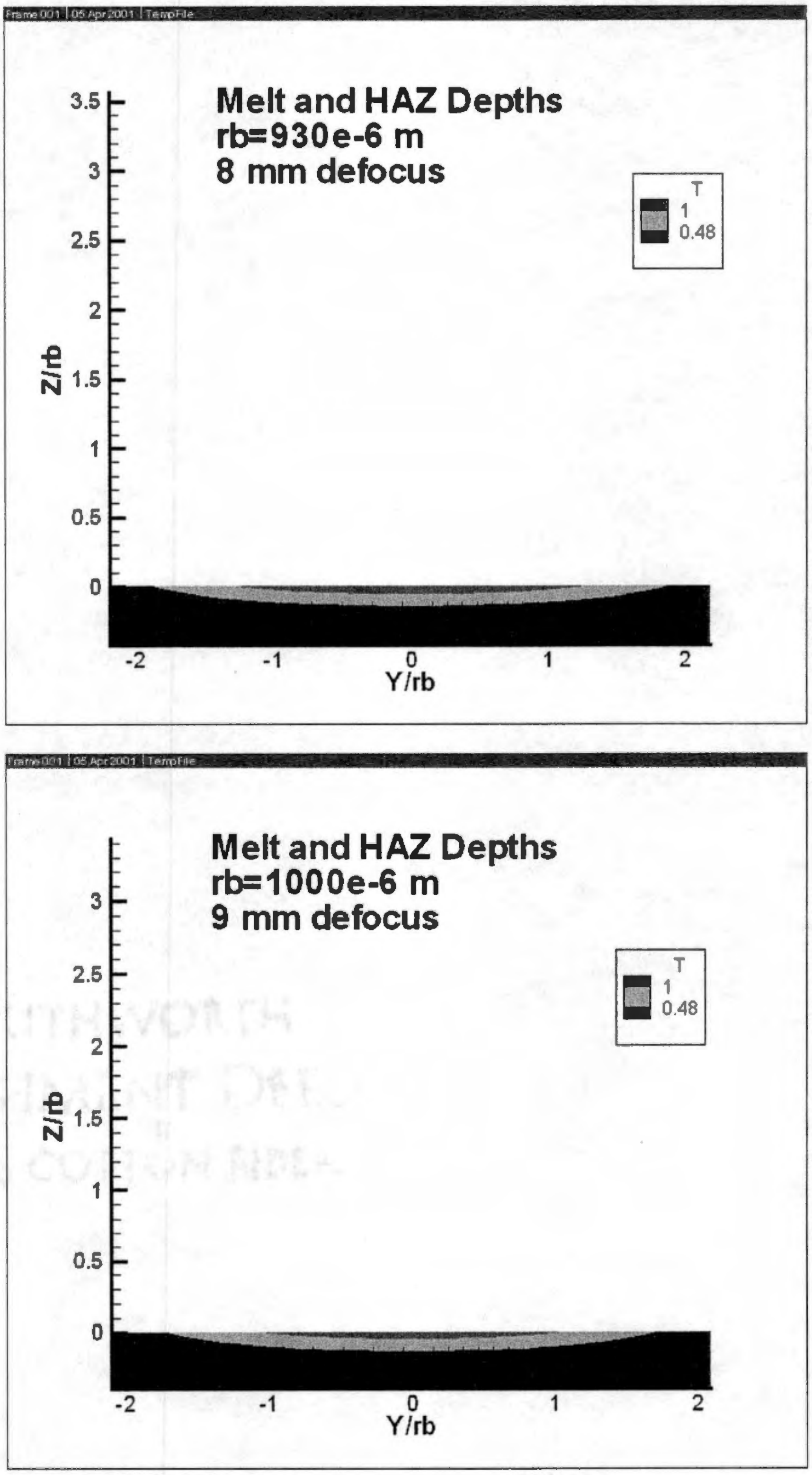

Figure 5.13 Melt and HAZ Profiles for -8 mm and -9 mm Defocus Distance at 2000 W, 5000 mm/min

depths were then multiplied by the normalization constant to obtain depths with dimensions of μm shown in numerical form in table 5.3 and in figure 5.14 as a function of defocus and intensity. The depths listed for the melt zone appear to be almost constant while the depths listed for the HAZ actually increase with an increase in the amount of defocus distance. Although this may seem counterintuitive, the beam translation rate, beam intensity, and energy diffusion rate all enter into the behavior of these curves, and under conditions in which the translation rate is relatively high compared to the interaction time and diffusion speed, the above behavior may be anticipated.

When comparing the simulation depths with experimental depths a difference in trends can be noted along with a difference in absolute melt depth as seen in figure 5.15. In order to better to provide a better understand these differences, the temperature simulation technique has been investigated.

5.9 Investigation of Temperature Simulation Technique

As noted in the previous section, the experimental and simulation melt and HAZ depth data differ in both trend and absolute values. An examination of the temperature simulation technique has been conducted to better evaluate the technique. The single Gaussian temperature simulation technique developed by Shercliff and Ashby (91) is investigated first in order to analyze its performance. Using the center source from the constructed beam profiles and a single Gaussian source with a radius equal to the center source's radius and its power matched to the total power of the experimental beam, melt and HAZ depth simulations were conducted. These depths can be seen in figure 5.15.

Table 5.3 Simulated Melt and HAZ Depths

Defocus Distance mm	Melt Zone Depth µm	HAZ Depth µm	Melt Depth /HAZ Depth
-0	68	108	0.630
-1	72	112	0.643
-2	68	113	0.602
-3	68	116	0.586
-4	64	116	0.552
-5	64	124	0.516
-6	60	124	0.484
-7	60	128	0.469
-8	52	128	0.406
-9	48	132	0.364

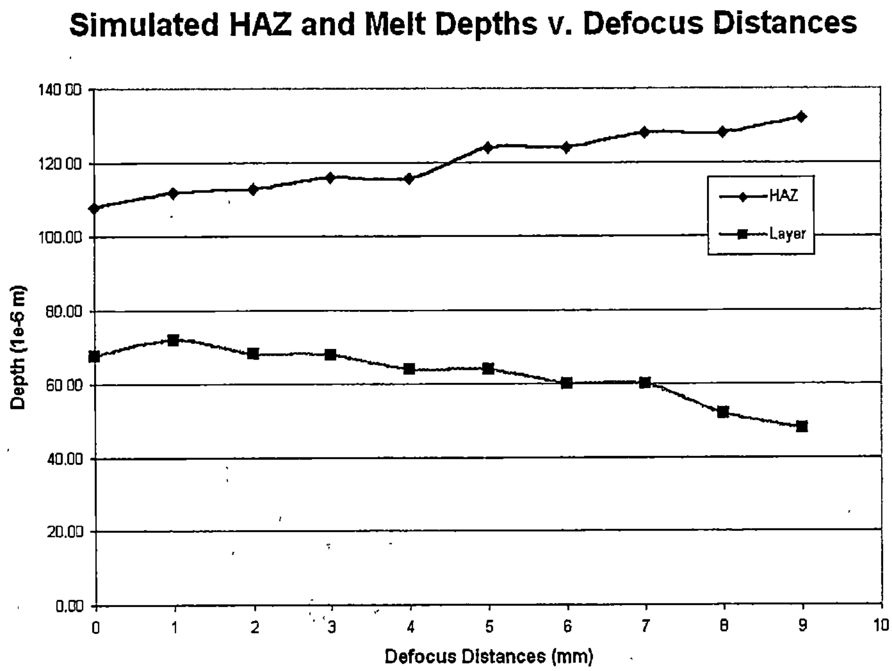

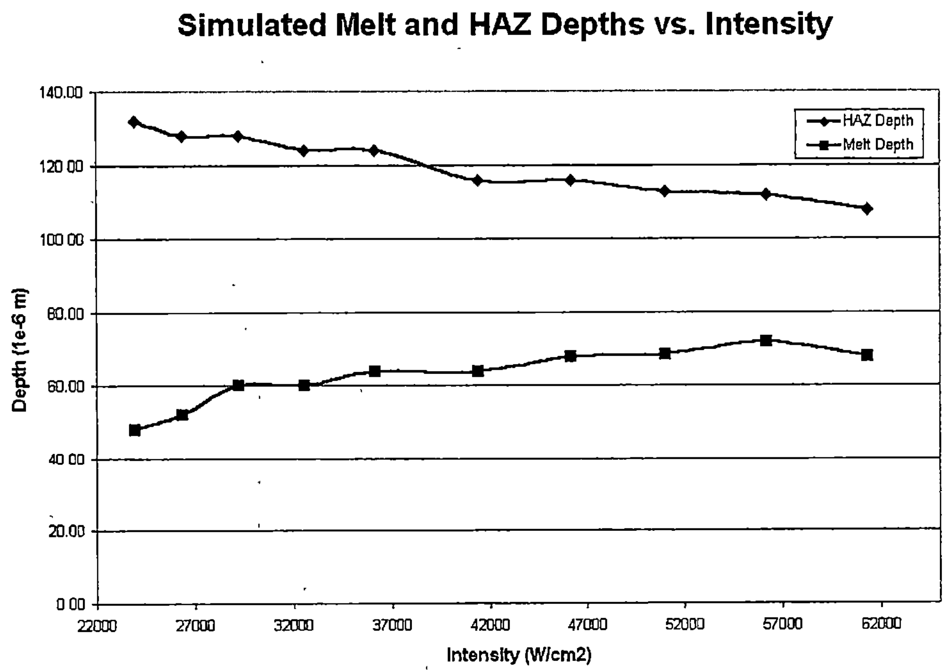

Figure 5.14 Simulation Melt and HAZ Depths as a Function of Defocus Distance and Intensity at 2000 W, 5000 mm/min

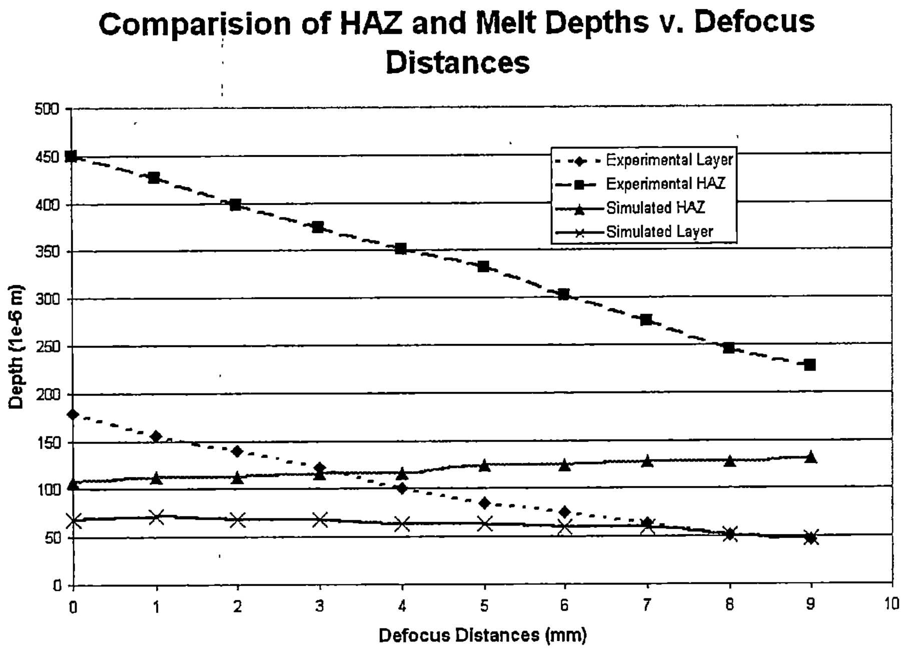

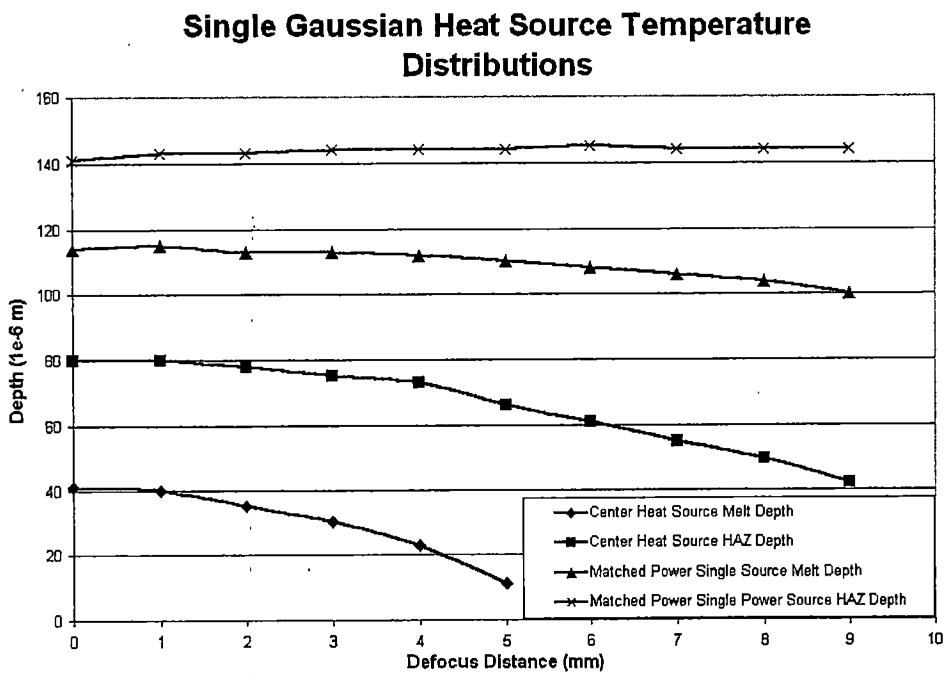

Figure 5.15 Comparison of Experimental and Simulation Results and Single Gaussian Source Melt and HAZ Depths at 2000 W, 5000 mm/min

As noted in the figure, the trends for the center source match more closely to those of the experimental measurements while the matched power source has a decreasing trend for the melt depth and an almost constant trend for the HAZ depth. However, the values do not match experimental results in either case. Next, the temperature depths for the –0 mm and –9 mm defocus distance case were examined for the center Gaussian source, matched Gaussian source, and the multiple source case. These depths are shown in figure 5.16 and figure 5.17. The plots for the single Gaussian source cases indicate little or no intersection in the temperature depth data while the multiple source case shows a distinct intersection. This data reveals a difference in the heat diffusion curves between the single Gaussian source and multiple source cases. The value of the characteristic length determines the general shape of these diffusion curves by dictating how quickly the heat diffuses in the material. The characteristic lengths and time to peak temperatures are listed in table 5.4. Thus, the method of the determination of these characteristic lengths is not satisfactory for the multiple source beam geometry simulation used in this research.

The difference in the absolute values was examined by using various input parameters to investigate their effect on simulated melt and HAZ depths. The absorptivity was increased to 1.5 for one trial, the thermal conductivity was increased to 38.4 for a second trial, the absorptivity was increased to 1.5 for the peak temperature calculation for a third trial, and the velocity was reduced to 3000 mm/min for a fourth trial. These depths are shown in figure 5.18. As noted in the figure, none of these modifications change the absolute values or trends drastically. This investigation of absolute values was continued for the specific case of –5 mm of defocus. Absorptivity values of 0.5, 1.0, 1.5, 2.0 and velocities of 500 mm/min, 3000 mm/min, and 5000

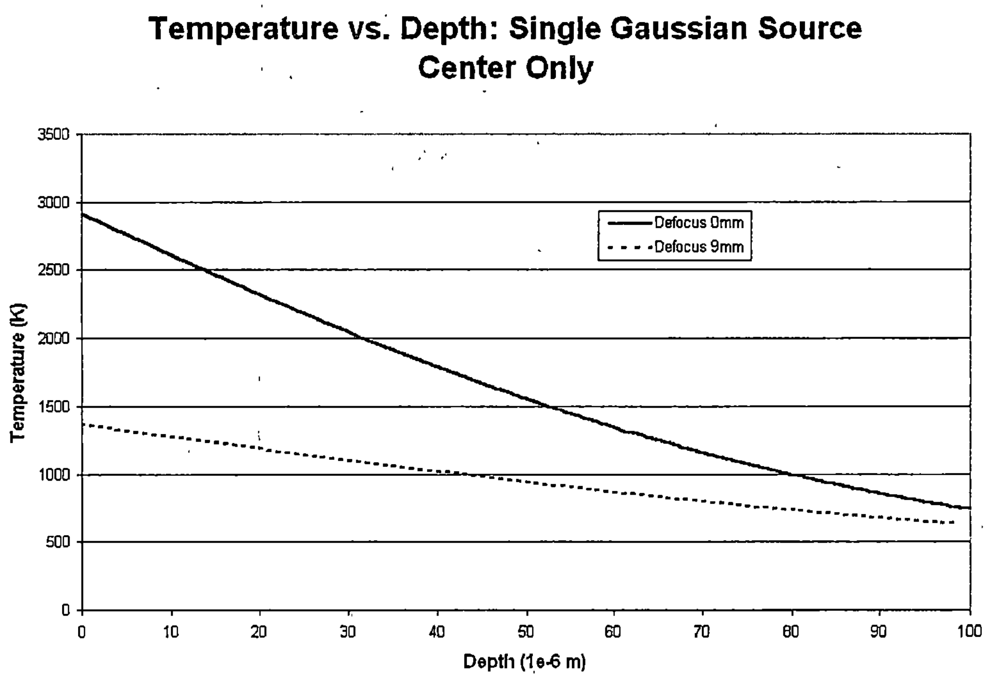

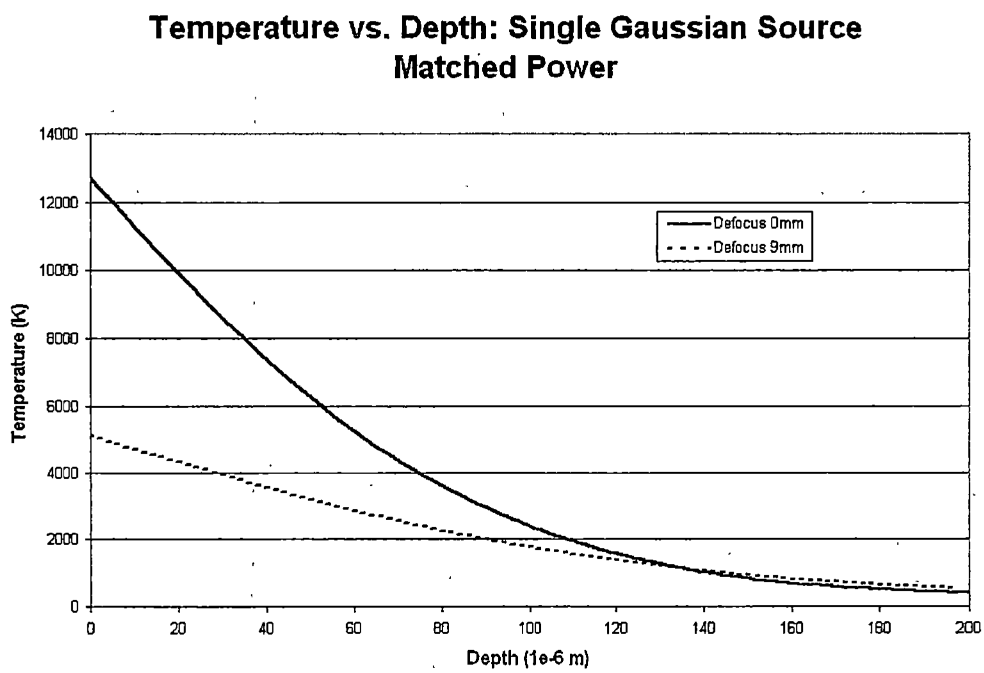

Figure 5.16 Temperature Depths for Single Gaussian Sources

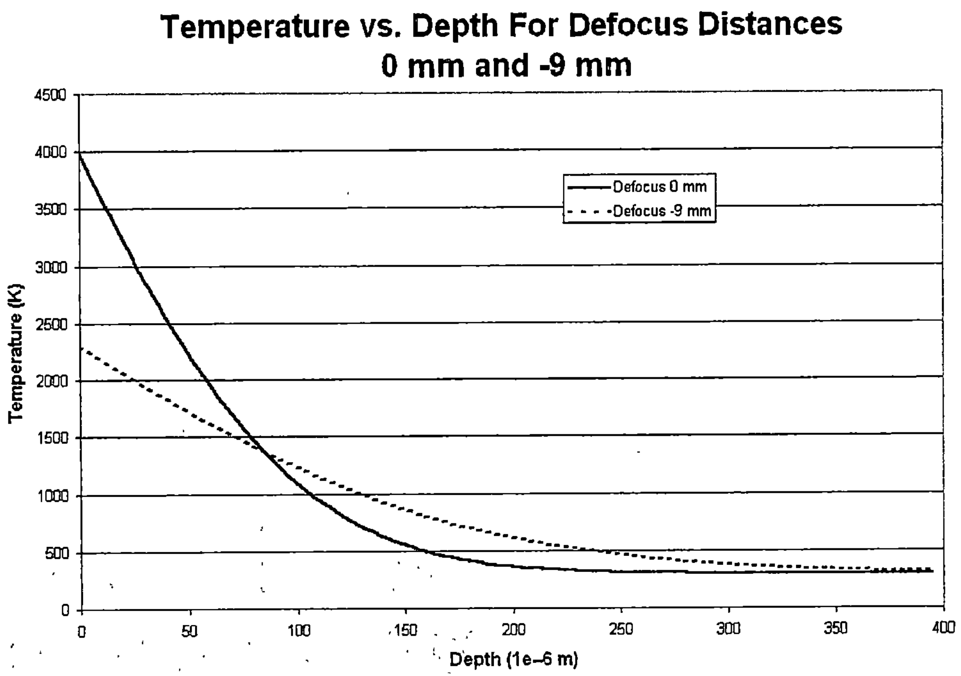

Figure 5.17 Temperature Depths for Multiple Source Case

Table 5.4 Time to Peak Temperature for Defocus Distances

Defocus Distance mm	Characteristic Length z_0 μm	Time to Peak Temperature ms
-0	103.83	1.40
-1	109.96	1.57
-2	114.55	1.70
-3	119.67	1.87
-4	127.18	2.11
-5	139.64	2.55
-6	148.25	2.88
-7	160.60	3.38
-8	168.87	3.74
-9	177.95	4.16

Modification to Simulation Parameters

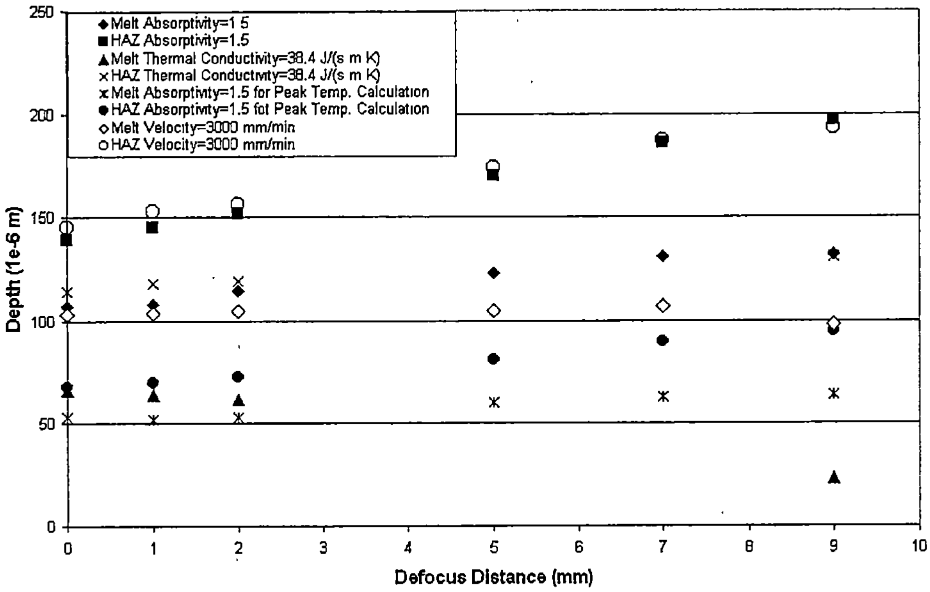

Case Depths For Various Beam Powers at -5 mm Defocus

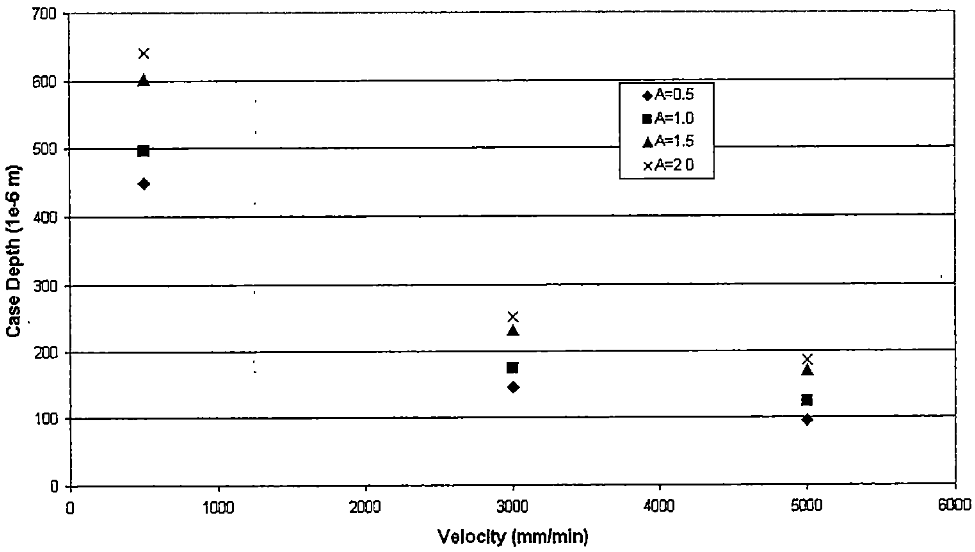

Figure 5.18 Modifications to Simulation Parameters and Case Depths For the –5 mm Defocus Distance Case at Various Beam Powers

mm/min were used in the simulation of HAZ or case depths shown in figure 5.18. The absorptivity variation in each velocity case shows little effect on the case depth while the case depth was significantly increased for the 500 mm/min velocity case, which are only 10% of the true processing velocity. These simulations show a poor prediction of the absolute values with little or no variation in the values for a change in input parameters in the immediate range of the actual parameters.

The fact that the peak temperature calculation used in the temperature simulations was predicted by a stationary rectangular beam approximation. The relationship of this peak temperature prediction with the defocus distance is shown in figure 5.19. This linear relationship agrees with the experimental values in trend. When the peak temperature is increased artificially as in figure 5.18, the melt and HAZ depth actually decrease. This, again, appears to be the result of the characteristic length being decreased to accommodate for the higher surface temperature. This method of the characteristic length once again appears to be unsatisfactory for the application used in this research. As a last examination of the temperature simulation technique, the dimensionless simulation and experimental case depths z^*_c were plotted against the dimensionless total beam power q^* shown in figure 5.19. The plots show the correct trend but contain an absolute value difference of around 164%-423%. These percentages compare with the multiple source rectangular beam error percentages in figure 8 in the work of Shercliff and Asbhy (91) which are around a maximum of 200% for a q* of 11.2.

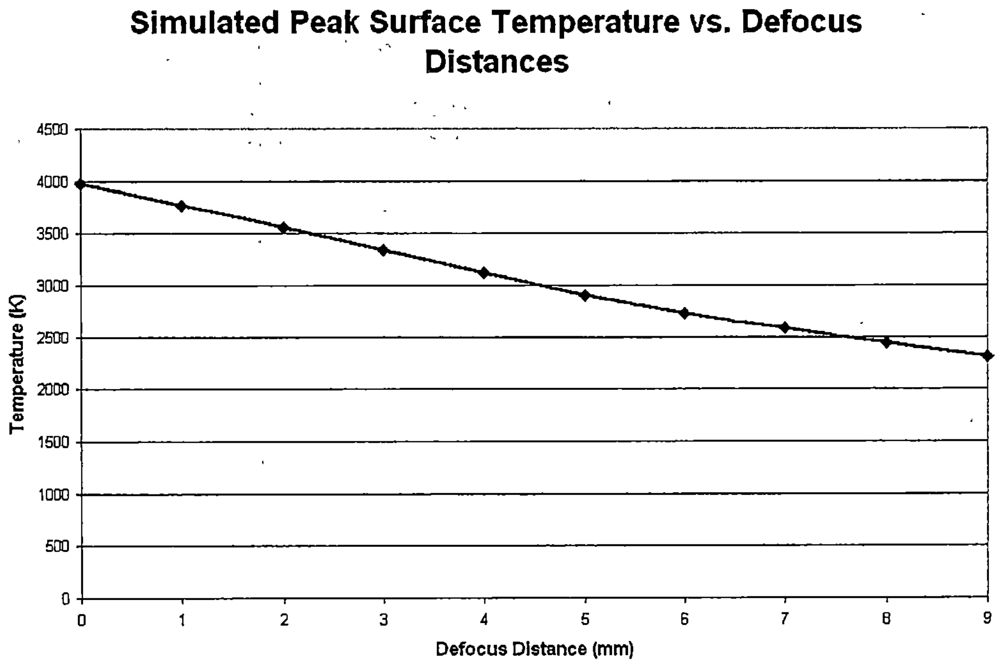

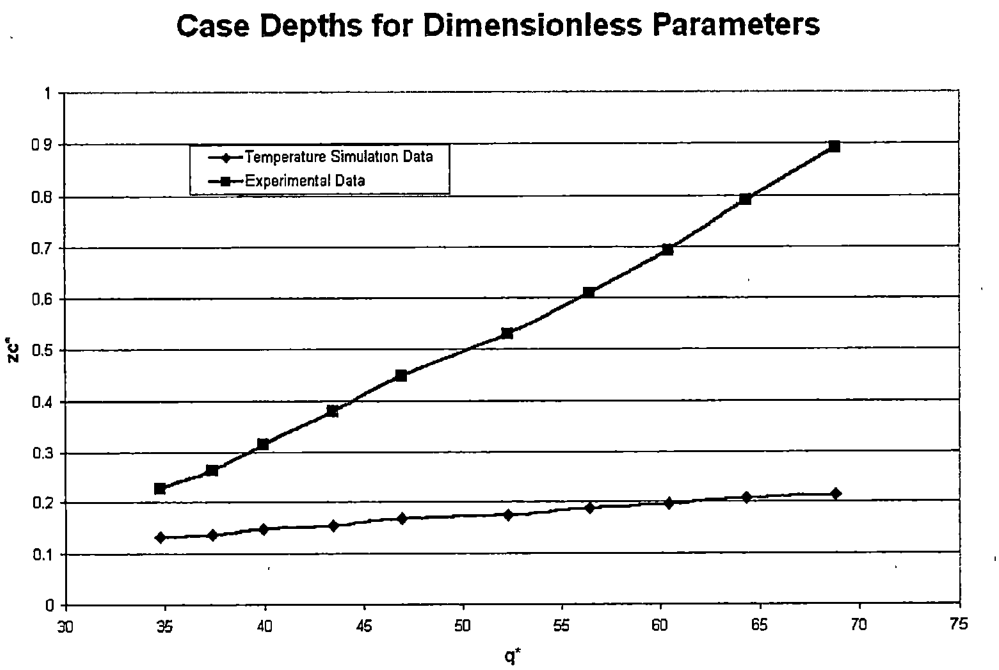

Figure 5.19 Simulated Peak Temperatures vs. Defocus Distances and Case Depths for Dimensionless Parameters

From this investigation, it can be seen that although this temperature simulation technique as applied to these conditions compares favorably to the calculations performed by Shercliff and Asbhy (91) in absolute value, it does not satisfactorily predict temperature distributions in trend because of inaccuracies in the diffusion curves.

Chapter 6

Conclusions and Recommendations

This final chapter contains concluding sections of this research, including key points and possible future work. The key points section highlights notable areas of discovery in this research, and the future work section suggests possible improvements.

6.1 Research Key Points

By investigating changes to final processing quality resulting for focus distances changes, several ideas were researched. The degradation of final processing quality as the result of defocusing for an elliptical laser beam profile was determined by comparing final processing characteristics such as geometry, processed layer depths, and HAZ depths and shown to have linear relationship of –13.3 μm/mm for the melt depth and -22.3 μm/mm for the HAZ depths. Similarly, the influence of intensity on depth was determined to be 3.57 μm/kW/cm^2 for the melt depth and about 5.97μm/kW/cm^2 for the HAZ depth. An increase in width across the processed track of the melt and HAZ regions was also noted as the depths of these regions became smaller. Required correction reaction dynamics were investigated to present a range of specifications encountered during focus distance correction and found to require a correction velocity of 4000 mm/min for defocus distance of –4 mm. The required horizontal resolution was found to be 3.5 times the radius of the surface variation encountered. The current hardware capability, with a maximum vertical velocity of 18300 mm/min, meets these velocity requirements. A temperature distribution simulation for laser surface treatments involving melting and non-Gaussian laser beam profiles has been implemented and shown to be unsuitable for the application used in this research. The values for melt and HAZ depths were in the error range of 164%-423% when compared to the experimental data, and although this may be adequate for some applications, it is below the accuracy required for implementation in a process control system. Melt and HAZ depth trends in relation to defocus distances were also shown to be inconsistent with observations for this application. A more accurate model is required for control system purposes.

6.2 Proposed Future Work

Future work could include the possible investigation of the influence on the relation of process quality and laser beam defocus for different processing velocities. Also, an automated focus correction system could be implemented and tested to determine its success. Finally, a more precise temperature simulation model could be investigated and implemented for use in focus correction system.

BIBLIOGRAPHY

BIBLIOGRAPHY

Aerotech Inc., *Motion Control Catalog Number 2*

Agarwala, R. P. editor., *Lasers in Material Science.* Switzerland: Trans Tech Publications, 1999.

Ashby, M. F. and Easterling, K. E., The Transformation Hardening of Steel Surfaces By Laser Beams – I. Hypo-Eutectoid Steels, *Acta. Metall.,* vol. 32 (11), 1984.

Bass, M., Laser Heating of Solids, *Physical Processes in Laser-Materials Interactions.* New York: Plenum Press, 1983.

Carslaw, H. S. and Jaeger J. C., *Conduction of Heat in Solids.* Second Edition. London: Oxford University Press, 1959.

Cline, H. E. and Anthony, T. R., Heat Treating and Melting Material With a Scanning Laser or Electron Beam, *J. Appl. Phys.,* vol. 48 (9), 1977.

Drazin, P. G. and Reid, W. H., *Hydrodynamic Stabilty.* Cambridge, United Kingdom: Cambridge University Press, 1981.

Charschan, S. S. editor., *Guide to Laser Materials Processing.* Orlando, Florida: Laser Institute of America, 1993.

Grigoryants, A. G., *Basics of Laser Material Processing.* Moscow: Mir Publishers, 1994.

Keyence website: *http://world.keyence.com/sensors/measurement/lasers/lk/lk_spec.html* July 2001.

Lax, M., Temperature Rise Induced by a Laser Beam, *J. Appl. Phys.,* vol. 48 (9), 1977.

Pedrotti, F. L. and Pedrotti, L. S., *Introduction to Optics.* Second Edition. Upper Saddle River, New Jersey: Prentice-Hall, Inc., 1993.

Ready, J. F., *Industrial Applications of Lasers.* Second Edition. San Diego: Academic Press, 1997.

D. Rosenthal. The Theory of Moving Sources of Heat and Its Application to Metal Treatments, *Trans. Am. Soc. Mech. Engrs.* vol 68, 1946.

Rykalin, N., Uglov, A., and Kokora, A., *Laser Machining and Welding.* Moscow: Mir Publishers, 1978.

Sanders, D. J., Temperature Distributions Produced By Scanning Gaussian Laser Beams, *Appl.Opt.*, vol. 23 (1), 1984.

Schwartz, F., (private communication), University of Tennessee Space Institute, Tullahoma, TN, November 2000.

Shercliff, H. R. and Ashby, M. F., The Prediction of Case Depth in Laser Transformation Hardening, *Metall. Trans. A.*, vol. 22A (10), 1991.

Silfvast, W. T., *Laser Fundamentals.* Cambridge, United Kingdom: Cambridge University Press, 1996.

Steen, P. H., Ehrhard, P., and Schussler, A., Depth of Melt-Pool and Heat-Affected Zone In Laser Surface Treatments, *Metall. Mat. Trans. A.* vol. 25A (2), 1994.

Techno-Isel, *Linear Motion Products Catalog H830*

Von Allmen, M. and Blatter, A., *Laser-Beam Interactions with Materials.* Berlin: Springer, 1995.

Wong, H. Y., *Handbook of Essential Formulae and Data on Heat Transfer for Engineers.* London: Longman Publishers, 1977.

VITA

Matthew Scott Anderson was born on September 11,1976, in Charlotte, Tennessee. He completed his primary education in Dickson County, Tennessee. He graduated from Dickson County Senior High School in May, 1995, and went on to complete a Bachelor of Science in physics form Austin Peay State University in May, 1999. He then received a Master of Science in Engineering Science in December 2001 from the University of Tennessee Space Institute in Tullahoma, TN.